Measurement-Based Analysis of MIMO Communications over the PCS Spectrum

by

Naveen N. Sunkavally

Submitted to the Department of Electrical Engineering and Computer Science
in partial fulfillment of the requirements for the degree of

Masters of Engineering in Electrical Engineering and Computer Science

at the

MASSACHUSETTS INSTITUTE OF TECHNOLOGY

May 2002
[June 2002]

Author .....
Department of Electrical Engineering and Computer Science
May 24, 2002

Certified by.....
Vahid Tarokh
Associate Professor
Thesis Supervisor

Accepted by.....
Arthur C. Smith
Chairman, Department Committee on Graduate Students

Measurement-Based Analysis of MIMO Communications over the PCS Spectrum

by

Naveen N. Sunkavally

Submitted to the Department of Electrical Engineering and Computer Science
on May 24, 2002, in partial fulfillment of the
requirements for the degree of
Masters of Engineering in Electrical Engineering and Computer Science

Abstract

The objective of this thesis is to design a system to analyze the real-world performance of space-time codes for narrowband multiple-input multiple-output (MIMO) communications. In theory, space-time codes, which are a form of coded modulation for high-rate multiple antenna systems, have been shown to bring about significant performance increases in terms of bit error probability over conventional uncoded systems. However, until now, not many experiments have verified the power of these codes in practice; most of the major preceding work has focused on understanding the nature of the MIMO channel and channel estimation ([1], [2], [3], [4]).

This thesis goes through the process of designing a MIMO system in conjunction with the Signals and Systems group at Lincoln Laboratories for an indoor field test at Lincoln Labs. In this field test, space-time coding schemes were tested for scenarios with up to 8 fixed transmit antennas and 10 fixed receive antennas. Preliminary analysis of the experimental data seems to suggest that space-time codes are indeed capable of achieving their theoretical potential.

Thesis Supervisor: Vahid Tarokh
Title: Associate Professor

Acknowledgments [1]

First and foremost, I am deeply grateful to my advisors, Vahid Tarokh at MIT and Dan Bliss at Lincoln Labs, for taking me on this project and for their kindness, enthusiasm, patience, and encouragement. I have truly learned an enormous amount under their guidance this past year.

I am indebted to my wise graduate student mentor Julius Kusuma, who gave me perspective and answered the questions I would have been embarrassed to ask otherwise. I also thank Dr. Il-Min Kim for breaking (and fixing) my code several times throughout the year.

I am grateful for group leader Gary Hatke for hiring me and the research staff at Lincoln Labs, including Ali Yegulalp and Nick Chang, for their help with channel estimation, and Keith Forsythe. I am of course also indebted to Lincoln's over-extended hardware and technical staff, including Sean Tobin, Jeff Nowak, Lee Duter, John Mann, Peter Priestner, and Bob Devine, for carrying out the experiment on which this thesis is based.

Finally, I thank my parents and brother, without whom none of this would have been possible in the first place.

[1] This work was sponsored by the Defense Advanced Research Projects Agency under Air Force Contract F19268-00-C-0002. Opinions, interpretations, conclusions, and recommendations are those of the author and are not necessarily endorsed by the United States Government.

Contents

List of Figures

Chapter 1

Introduction

The objective of this thesis is to design a system to analyze the real-world performance of space-time codes for narrowband multiple-input multiple-output (MIMO) communications. In theory, space-time codes, which are a form of coded modulation for high-rate multiple antenna systems, have been shown to bring about significant performance increases in terms of bit error probability over conventional uncoded systems. However, until now, not many experiments have verified the power of these codes in practice; most of the major preceding work has focused on understanding the nature of the MIMO channel and channel estimation ([1], [2], [3], [4]).

This thesis goes through the process of designing a MIMO system in conjunction with the Signals and Systems group at Lincoln Laboratories for an indoor field test at Lincoln Labs. In this field test, space-time coding schemes were tested for scenarios with up to 8 fixed transmit antennas and 10 fixed receive antennas. Preliminary analysis of the experimental data seems to suggest that space-time codes are indeed capable of achieving their theoretical potential.

This paper is divided into five chapters. Chapters I and II provide background information necessary to start the experiment. The first chapter discusses the MIMO system model under consideration for this project and also looks at the capacity for such a system. Chapter II introduces space-time codes and analyzes the performance of space-time block and trellis codes; simulation results relevant to the Lincoln experiment are also presented.

Chapter III discusses the experimental setup, and Chapter IV covers pulse-shaping and the receiver front end. Finally, Chapter V goes through the preliminary analysis and draws

conclusions.

1.1 The MIMO System Model

In this section a simple model for the MIMO system is presented. While many of the assumptions underlying the model are gross simplifications and do not hold in the real-world, the model is nonetheless useful for establishing benchmarks via simulations.

The model is for a multiple-antenna QAM system consisting of an uninformed transmitter equipped with n_T transmit antennas and a receiver equipped with n_R receive antennas. The receiver is assumed to have perfect channel state information (CSI). The transmit antennas are synchronized and transmit with symbol period T. The path from transmit antenna i to receive antenna j is assumed to be decorrelated with all other transmit-receive antenna paths.

Under the discrete-time lowpass model, each transmit antenna i, $1 \leq i \leq n_T$, has a stream of symbols it wishes to transmit of the form $c_i^1, c_i^2 \ldots c_i^t, c_i^{t+1} \ldots c_i^{t+2} \ldots$, where t is a discrete index over time. Let C denote the matrix of symbols sent from all transmit antennas over a time interval $1 \leq t \leq l$:

$$C = \begin{pmatrix} c_1^1 & c_1^2 & \ldots & c_1^l \\ c_2^1 & c_2^2 & \ldots & c_2^l \\ \vdots & \vdots & \ddots & \vdots \\ c_{n_T}^1 & c_{n_T}^2 & \ldots & c_{n_T}^l \end{pmatrix}$$

In general the stream of symbols for each transmit antenna may or may not be part of the same signal constellation, and they may not have the same average energy; however, for an uninformed transmitter (i.e. no feedback from the receiver), the best strategy is to expend equal power on all transmit antennas. The symbols c_i^t have been normalized to have unit energy, and E_s denotes the average energy per symbol (the same for all transmit antennas).

The channel is assumed to be quasi-static, Rayleigh, and flat fading, with additive white Gaussian noise (AWGN) at each receive antenna. The channel matrix H can be modeled as consisting of independent Rayleigh flat fading complex gain coefficients $\alpha_{i,j}$, which represent the gain from transmit antenna i to receive antenna j, $1 \leq j \leq n_R$. The term "flat fading"

means that the subchannel from one antenna to another can be characterized by one tap, i.e. the length of any subchannel response is shorter than T. In the frequency domain, "flat fading" indicates that transmission is taking place over a narrow enough portion of the spectrum that the channel frequency response over that portion can be modeled as roughly constant. The channel is assumed to be constant over the duration of a frame's worth of data, and to change independently between frames.

$$H = \begin{pmatrix} \alpha_{1,1} & \alpha_{2,1} & \cdots & \alpha_{n_T,1} \\ \alpha_{1,2} & \alpha_{2,2} & \cdots & \alpha_{n_T,2} \\ \vdots & \vdots & \ddots & \vdots \\ \alpha_{1,n_R} & \alpha_{2,n_R} & \cdots & \alpha_{n_T,n_R} \end{pmatrix}$$

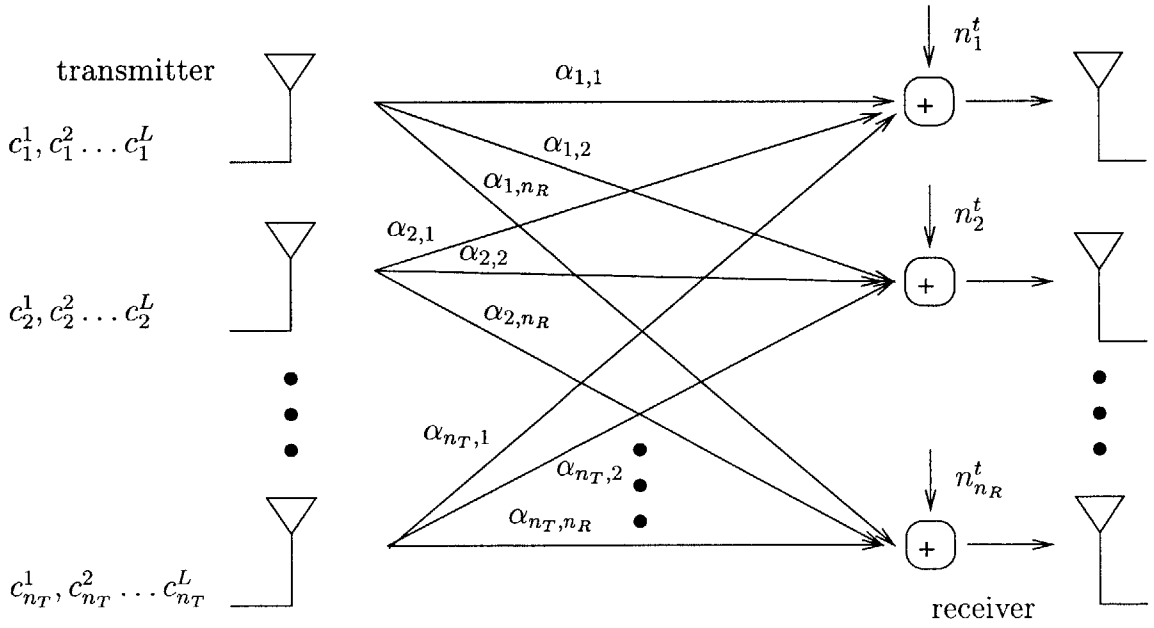

Figure 1-1: *Idealized MIMO system*

For the purpose of simulations, the $\alpha_{i,j}$ are normalized to have variance $\frac{1}{2}$ per real dimension; in other words the channel is normalized so that on average there is no gain in the path from any transmit antenna to any receive antenna.

The noise at each receive antenna is modeled as AWGN with variance $\frac{N_o}{2}$ per real dimension. Let N denote the matrix of noise terms n_j^t for $1 \leq t \leq l$.

$$N = \begin{pmatrix} n_1^1 & n_1^2 & \dots & n_1^l \\ n_2^1 & n_2^2 & \dots & n_2^l \\ \vdots & \vdots & \ddots & \vdots \\ n_{n_R}^1 & n_{n_R}^2 & \dots & n_{n_R}^l \end{pmatrix}$$

Figure 1-1 illustrates the system under consideration. Each receive antenna j receives a linear combination of the signals from each transmit antenna weighted by the channel gains to j, plus some noise. The received signal matrix R can be represented as:

$$R = \sqrt{E_s}HC + N$$

The received signal for the jth receive antenna at timestep t equals:

$$r_j^t = \sum_{i=1}^{n_T} \alpha_{i,j} c_i^t \sqrt{E_s} + n_j^t$$

1.1.1 Deviations from the Ideal System Model

The real-world departs from the simple channel model above in several significant ways:

- Quasi-static fading: A real channel is not constant for a period of time only to change independently afterwards. Physical channels are always changing, either slowly or quickly, and there is usually a great amount of correlation between the value of the channel at one time instant to the value at the next time instant. Depending on how quickly the channel is changing, the quasi-static fading assumption or may or may not be valid. In Chapter V, it is shown that the channel for the Lincoln indoors field test changed slowly enough that the quasi-static fading assumption is a fairly good approximation.

- Perfect CSI: The receiver in practice must estimate the channel either with training sequences and/or iteratively with the data itself. In Chapter V, the first frame of data is used as a training sequence to estimate the channel; subsequent frames are decoded iteratively, and the channel estimate is modified frame by frame.

- Subchannel decorrelation: In reality, the path from a specific transmit antenna to

a specific receive antenna is correlated with every other transmit-receive path. The degree of correlation depends on how far the transmit antennas are spaced and the richness of scatterers in the environment. Reference [1] shows that spatial decorrelation (cross-correlation less than .8) may be achieved with transmit antenna spacing anywhere between one-third of a wavelength of the carrier frequency to 30 wavelengths.

- AWGN noise and Rayleigh fading: Noise in real systems is never exactly AWGN; for the Lincoln experiment, irregularities in the noise were found in the form of "spurs", or noisy tones, and temporal and spatial correlation. Similarly, channel coefficients don't exactly arise from a Rayleigh distribution.

1.2 MIMO System Capacity

1.2.1 Telatar/Foschini Estimate

Telatar [5] and Foschini [6] show that the ergodic capacity C in bits/s/Hz, assuming the simple channel model described above, takes the form:

$$C = E_H\{\log_2(|I_{n_R} + \frac{SNR}{n_T} HH^*|)\}$$

SNR equals $\frac{P}{N_o}$, where $P = n_T E_s$ is the total transmit energy at an instant in time. I_{n_R} is an identity matrix with n_R rows and columns. H^* denotes the Hermitian conjugate of H. The $||$ operator denotes the determinant operator. E_H denotes the expectation over all realizations of the channel matrix H.

In [5], the expectation is evaluated explicitly by looking at the probability density function of the eigenvalues of H. A major result of that paper and [6] is that the capacity at high SNR increases at least linearly with the minimum number of transmit and receive antennas, i.e. $\min\{n_T, n_R\}$, assuming the channel model described above. The capacity also increases logarithmically with SNR. The ergodic capacity is plotted in Figure 1-2.

It is seen from the graph that a 3 dB increase in SNR corresponds to roughly an increase in capacity of $n_T = n_R$ bits/s/Hz.

For the Lincoln indoors field test, with all antennas stationary, the Telatar/Foschini estimate provides a reasonable upper bound on the performance that can be expected for the Lincoln system.

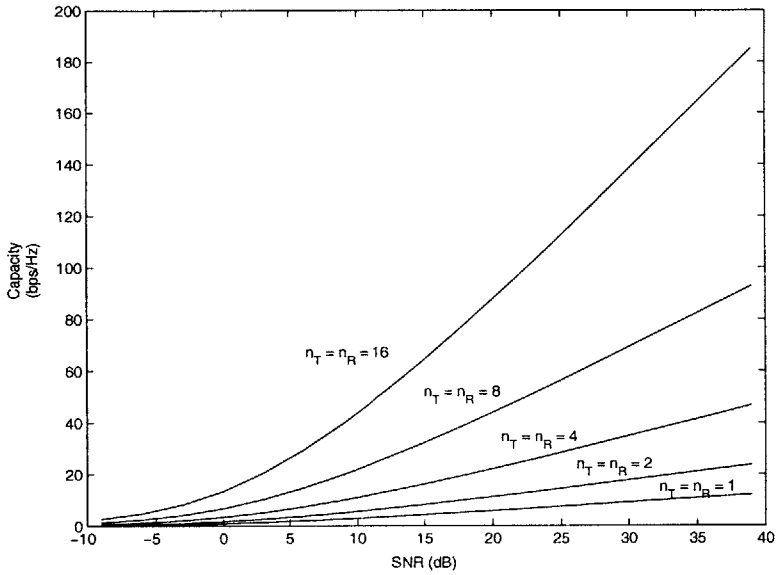

Figure 1-2: *Ergodic capacities for different $n_T = n_R$ values*

Chapter 2

Space-Time Block and Trellis Codes

Space-time codes are a form of coded modulation designed for transmitters with multiple transmit antennas. The codes achieve bit rates closer to capacity by exploiting spatial diversity, or redundancy, in the form of multiple transmit-receive paths. For this thesis integration of the space-time coding block into the physical layer occurs after the error-correction coding block as illustrated in figure 2-1. The signal constellation S is assumed to be Gray-labeled. As shown in [7] and [8], such an arrangement, in which forward error correction is separated from channel encoding and constellations are Gray-labeled, promotes modularity while still giving better BER performance on the fading channel than other schemes which have been developed in the Ungerboeck [9] set-partitioning framework. The space-time coding block is responsible for mapping the input bits to symbols in the signal constellation $\mathcal{S}$ in conjunction with converting those symbols from serial to parallel onto the n_T transmit antennas.

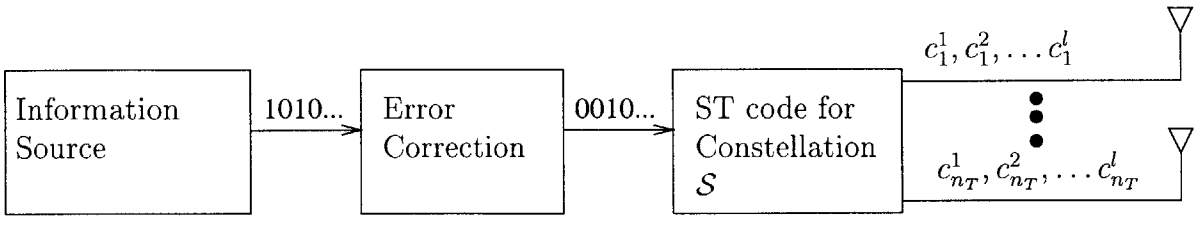

Figure 2-1: *Integration of space-time coding into transmit-side physical layer*

In this chapter, criteria are first presented for good space-time codes as established in [10] by Tarokh et al. for the ideal quasi-static Rayleigh flat fading model. A space-time code specifies how the conversion of serial to parallel is to take place for a particular signal constellation $\mathcal{S}$. The criteria quantify two characteristics that determine the performance of any space-time code: the diversity gain and the coding gain. It will be seen that one form of space-time coding, orthogonal space-time block codes (OSTBC), provide maximum diversity gain while being especially easy to decode. Space-time trellis codes, on the other hand, are harder to decode but can provide significant coding gain in addition to maximum diversity gain. Along the way, simulation results are presented for the relevant experiments that were performed at Lincoln Labs.

2.1 Establishing Benchmarks

Before discussing space-time codes, it is instructive to view simulations of the performance that can be expected on a single-input single-output (SISO) channel for the uncoded case over a fading channel. Figure 2-2 serves as a reference for the bit error rate (BER) performance that can be achieved using uncoded BPSK, 4-PSK, 8-PSK, 16-QAM, and 64-QAM. The BER is plotted as a function of SNR per symbol.

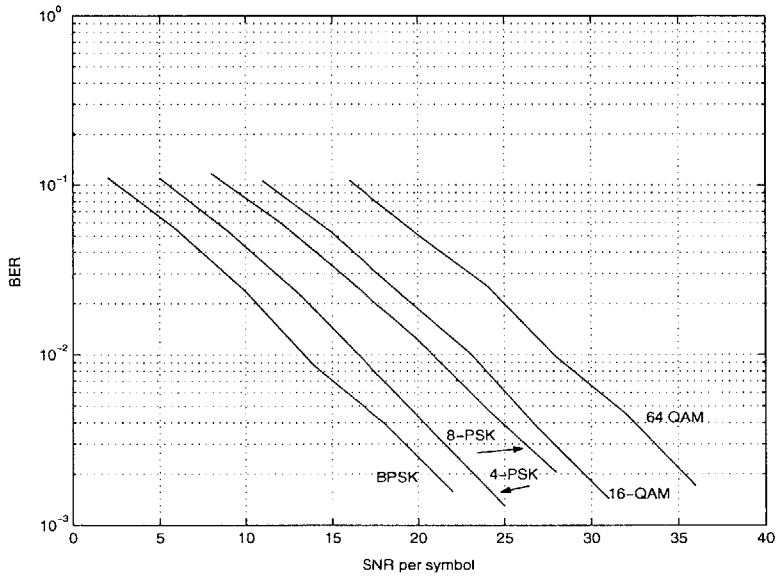

Figure 2-2: *Uncoded BER performance for different signal constellations*

All signal constellations above have been Gray-coded, and the receiver performs maximum-

likelihood decoding. As expected, if the average signal constellation energy is kept the same, constellations with larger minimum distance perform better, at the cost of less spectral efficiency. In addition, it is noteworthy that the performance of BPSK and 4-PSK is exactly the same when the bit error rate is plotted as a function of SNR per bit. (their performances differ by 3 dBs in Figure 2-2).

2.2 Space-Time Codes Criteria

Reference [10] describes two criteria for building good space-time codes over a MIMO Rayleigh fading channel, as shown in Figure 1-1. Consider two code matrices C and E for the discrete time interval $1 \leq t \leq l$, and define the difference matrix $B(C,E)$:

$$B(C,E) = C - E = \begin{pmatrix} c_1^1 - e_1^1 & c_1^2 - e_1^2 & \dots & c_1^l - e_1^1 \\ c_2^1 - e_2^1 & c_2^2 - e_2^2 & \dots & c_2^l - e_2^l \\ \vdots & \vdots & \ddots & \vdots \\ c_{n_T}^1 - e_{n_T}^1 & c_{n_T}^2 - e_{n_T}^2 & \dots & c_{n_T}^l - e_{n_T}^l \end{pmatrix}$$

Let λ_i, $1 \leq i \leq n_T$, represent the eigenvalues of $A(C,E) = B(C,E)B^*(C,E)$. Then [10] shows that the pairwise probability of confusing C for E at the receiver is upper-bounded by:

$$P(C \rightarrow E) \leq \left(\frac{1}{\prod_{i=1}^{n_T} (1 + \frac{\lambda_i E_s}{4N_o})} \right)^m$$

.

A more useful expression can be obtained if the eigenvalues are ordered from greatest to least and r is used to represent the number of non-zero eigenvalues (it is shown in [10] that all eigenvalues of A must be non-negative because of the existence of the square-root matrix B):

$$P(C \rightarrow E) \leq \left(\prod_{i=1}^{r} \lambda_i \right)^{-n_R} \left(\frac{E_s}{4N_o} \right)^{-rn_R}$$

.

The *diversity advantage* is defined as rn_R, and the *coding advantage* is defined as

$(\lambda_1 \lambda_2 \ldots \lambda_r)^{1/r}$. For a BER performance curve plotted vs. SNR in dBs, the diversity advantage controls the slope of the curve while the coding advantage controls the curve's position or relative displacement. The two criteria for Rayleigh space-time codes are:

- *The Rank Criterion*: In order to achieve the maximum diversity $n_T n_R$, the matrix $B(C,E)$ has to be full rank for any codewords C and E. If $B(C,E)$ has minimum rank r over the set of two tuples of distinct codewords, then a diversity of rn_R is achieved.

- *The Determinant Criterion*: Suppose that a diversity benefit of rn_R is the target. The minimum rth roots of the sum of the determinants of all $r \times r$ principal cofactors of $A(C,E) = B(C,E)B^*(C,E)$ taken over all pairs of distinct code matrices C and E corresponds to the coding advantage, where r is the rank of $A(C,E)$. Special attention in the design must be paid to this quantity for any code matrices C and E. The design target is making this sum as large as possible. If a diversity of $n_T n_R$ is the design target, then the minimum of the determinant of A(C, E) taken over all pairs of distinct codewords C and E must be maximized.

There are good intuitive explanations for the rank and determinant criteria. The rank criterion specifies that in order to maximize the diversity of a code, the minimum rank over all error matrices for all pairs of matrices C and E must be maximized. As the power at the transmitter is increased, the greater the rank, the more dimensions the error has to expand in; in general, the more dimensions that are available for the error to expand in, the greater the achievable distance is between any two code matrices.

The determinant criterion says that the minimum volume over the r dimensions under consideration must be maximized over all difference matrices. The product of the r non-zero eigenvalues correspond exactly to this volume measurement. Again, in general, the greater the minimum volume, the greater the minimum distance is between any two code matrices.

2.2.1 The Euclidean Distance Criterion

The criteria above are general but difficult to design codes around. A more simple criterion for designing space-time codes would be to simply maximize the minimum Euclidean distance $B(C,E)B^*(C,E)$ between all distinct code matrices C and E.

In [11] it is shown that the Euclidean distance criterion is indeed a valid metric to design codes around when the product rn_R is greater than 3. It shown that when $rn_R \geq 3$, the pairwise error probability between C and E is upper-bounded by:

$$P(C \rightarrow E) \leq \frac{1}{4} exp\left(-n_R \frac{E_s}{4N_o} \sum_{i=1}^{n_T} \lambda_i\right)$$

The condition $rn_R \geq 3$ implies that, if $n_T n_R \geq 3$, the Euclidean distance criterion can be used to design space-time codes. This also holds whenever $n_T \geq 3$. In [12] trellis codes are designed for the case $n_T \geq 3$ based on the Euclidean distance criterion.

2.3 Orthogonal Space-Time Block Codes

Orthogonal space-time block codes (OSTBCs) are a form of space-time coding in which the data transmitted from each transmit antenna in a block is orthogonal to data from every other transmit antenna in that block. An OSTBC system can be represented as a sequence of two blocks, the first of which serves to convert the input bit stream to symbols via a signal constellation $\mathcal{S}$ and the second of which performs the appropriate serial to parallel conversion. This second serial-to-parallel conversion block can be represented as a $n_T \times l$ matrix G, where l represents the block length in units of time. The code rate is defined as $\frac{k}{l}, where k is the number of input symbols that G accepts per block.$

For example, one OSTBC code matrix used in the Lincoln experiment specifically for two transmit antennas is the well-known rate 1 Alamouti code [13].

$$G_2 = \begin{pmatrix} x_1 & -x_2^* \\ x_2 & x_1^* \end{pmatrix}$$

The function of the G_2 matrix is as follows: after the bit-to-symbol map, the G_2 matrix takes in symbols two at a time, represented as x_1 and x_2. At time slot 1, the first symbol and the second symbol are sent by transmit antenna 1 and 2, respectively. At time slot 2, transmit antenna 1 sends the negative conjugate of the second symbol, and transmit antenna 2 sends the conjugate of the first symbol. It is clear that the sequence of symbols sent from antenna 1 is orthogonal to the sequence sent from antenna 2.

If the signal constellation $\mathcal{S}$ is the 4-PSK constellation, then there are 16 possible matri-

ces that would be sent from the two transmit antennas. By inspection of all possible pairs of difference matrices $B(C,E)$, it is observed that there exists no $B(C,E)$ of rank less than 2, and that the minimum determinant of a matrix $A(C,E) = B(C,E)B^*(C,E)$ is 1 (here the G_2 matrix has been normalized appropriately in order to make the average received energy per symbol at the receiver equal to 1; see the subsection on SNR calculation for more information). Thus, the diversity gain of the Alamouti code is $2n_R$ and the coding gain equals 1.

Other OSTBC matrices used for the Lincoln experiment are the rate $\frac{3}{4}$ H_4 matrix for four transmit antennas, and the rate $\frac{1}{2}$ G_8 matrix for eight transmit antennas. The H_4 matrix is given in [14], and the G_8 matrix is constructed from the real orthogonal design in [15]. It is also shown in [15] that no complex rate 1 square OSTBC matrix exists for more than two transmit antennas, and no real rate 1 square OSTBC matrix exists for more than eight transmit antennas.

$$H_4 = \begin{pmatrix} x_1 & -x_2^* & \frac{x_3^*}{\sqrt{(2)}} & \frac{x_3^*}{\sqrt{2}} \\ x_2 & x_1^* & \frac{x_3^*}{\sqrt{(2)}} & -\frac{x_3^*}{\sqrt{2}} \\ \frac{x_3}{\sqrt{2}} & \frac{x_3}{\sqrt{2}} & \frac{(-x_1-x_1^*+x_2-x_2^*)}{2} & \frac{(x_2+x_2^*+x_1-x_1^*)}{2} \\ \frac{x_3}{\sqrt{2}} & -\frac{x_3}{\sqrt{2}} & \frac{(-x_2-x_2^*+x_1-x_1^*)}{2} & \frac{(x_1+x_1^*+x_2-x_2^*)}{2} \end{pmatrix}$$

$$G_8 = \begin{pmatrix} x_1 & -x_2 & -x_3 & -x_4 & -x_5 & -x_6 & -x_7 & -x_8 & x_1^* & -x_2^* & -x_3^* & -x_4^* & -x_5^* & -x_6^* & -x_7^* & -x_8^* \\ x_2 & x_1 & -x_4 & x_3 & -x_6 & x_5 & x_8 & -x_7 & x_2^* & x_1^* & -x_4^* & x_3^* & -x_6^* & x_5^* & x_8^* & -x_7^* \\ x_3 & x_4 & x_1 & -x_2 & -x_7 & -x_8 & x_5 & x_6 & x_3^* & x_4^* & x_1^* & -x_2^* & -x_7^* & -x_8^* & x_5^* & x_6^* \\ x_4 & -x_3 & x_2 & x_1 & -x_8 & x_7 & -x_6 & x_5 & x_4^* & -x_3^* & x_2^* & x_1^* & -x_8^* & x_7^* & -x_6^* & x_5^* \\ x_5 & x_6 & x_7 & x_8 & x_1 & -x_2 & -x_3 & -x_4 & x_5^* & x_6^* & x_7^* & x_8^* & x_1^* & -x_2^* & -x_3^* & -x_4^* \\ x_6 & -x_5 & x_8 & -x_7 & x_2 & x_1 & x_4 & -x_3 & x_6^* & -x_5^* & x_8^* & -x_7^* & x_2^* & x_1^* & x_4^* & -x_3^* \\ x_7 & -x_8 & -x_5 & x_6 & x_3 & -x_4 & x_1 & x_2 & x_7^* & -x_8^* & -x_5^* & x_6^* & x_3^* & -x_4^* & x_1^* & x_2^* \\ x_8 & x_7 & -x_6 & -x_5 & x_4 & x_3 & -x_2 & x_1 & x_8^* & x_7^* & -x_6^* & -x_5^* & x_4^* & x_3^* & -x_2^* & x_1^* \end{pmatrix}$$

Again, both the H_4 and G_8 codes provide the maximum diversity of $4n_R$ and $8n_R$, respectively.

2.3.1 Decoding Orthogonal Space-Time Block Codes

One of the primary advantages of using orthogonal space-time block codes is that they provide maximum diversity while being easy to decode at the receiver. As shown in [15], the receiver only needs to use linear processing, and, instead of performing joint estimation over all k symbols per block, the receiver can decode each symbol separately. In effect, the orthogonality, assuming $n_T = n_R$, allows the MIMO system to become equivalent to a system of $n_T = n_R$ parallel, decoupled channels.

Reference [16] presents a modified version of the linear-processing decoding algorithm presented in [15]. In simulations, this algorithm is used for its generality and efficiency; a new decoding rule does not need to be derived for every new OSTBC. The basic idea behind the algorithm is to combine the channel matrix and the OSTBC code matrix into one super-matrix acting on the k input symbols.

Simulation results for the G_2, H_4, and G_8 cases are shown in Figure 2-3. For the G_2 case, the 4-PSK constellation is used and there are two receive antennas; for the H_4 case, the 16-QAM constellation is used and there are four receive antennas; and for the G_8 case, the 64-QAM constellation is used and there are eight receive antennas. The first case corresponds to an overall spectral efficiency of 2 bits/sec/Hz, the second case a spectral efficiency of 3 bits/sec/Hz, and the third case also a spectral efficiency of 3 bits/sec/Hz. These simulations mirror scenarios that were tested in the Lincoln indoor field test.

One result that can be seen clearly from Figure 2-3 is that scenarios with space-time codes give a significant performance advantage over uncoded scenarios. In addition, the three scenarios with space-time coding in the figure all perform more or less about the same, though in general, the lower the spectral efficiency, the better the bit error rate that can be expected.

SNR Calculation for OSTBC codes

It is useful to briefly discuss how to compute the SNR that is shown on the x-axis of figure 2-3. The SNR represented on the x-axis of those figures is the average SNR per symbol per receive antenna. Let R_j^p represent the received vector of data at the jth receive antenna for the pth block:

$$R_j^p = \{r_j^{1+p(l-1)}, r^{2+p(l-1)}, \ldots r_j^{l+p(l-1)}\}$$

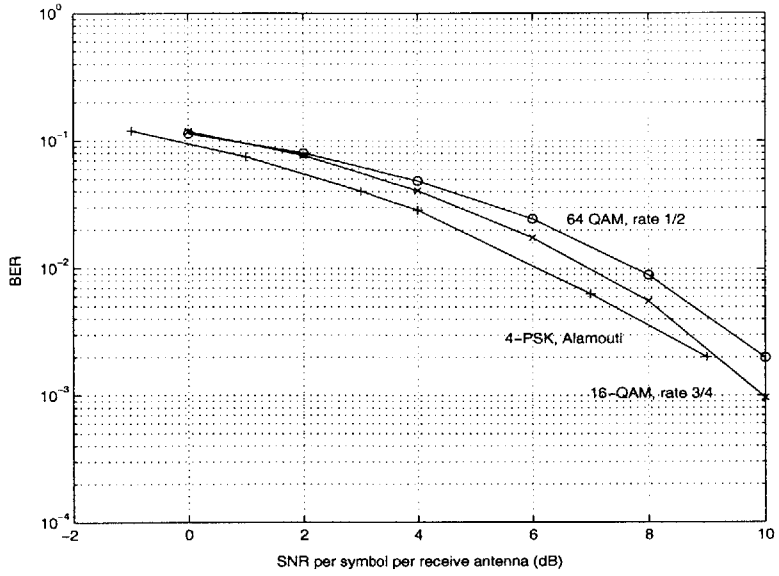

Figure 2-3: *Performance of different space-time orthogonal block codes*

where

$$r^{k+p(l-1)} = \sum_{i=1}^{n} \alpha_{i,j} c_i^{k+p(l-1)} + n_j^{k+p(l-1)}, k = 1 \ldots l$$

Here, the $c_i^{k+p(l-1)}$ have not been normalized to have unit energy, as they were in chapter 1; however, the $\alpha_{i,j}$ are still normalized to have unit variance per complex dimension and the noise terms have variance N_o per complex dimension.

The SNR can be calculated by taking the expectation of the inner product of R_j^p. Because the channel coefficients are independent and normalized to unit variance, and because the noise terms are also independent from each other and the channel coefficients, the SNR comes out to:

$$SNR = \frac{\frac{1}{l}\sum_{k=1}^{l}\sum_{i=1}^{n_T} |c_i^{k+p(l-1)}|^2}{N_o}$$

The SNR does not depend on the rate of the OSTBC code. For the sake of simulations, the total signal energy given in the numerator above is normalized to 1, and the noise variance is varied.

When dealing with real data, the SNR is calculated differently because it would be incorrect to assume that the channel coefficients are decorrelated and the noise is AWGN.

SNR calculation for real data is discussed in Chapter V.

2.4 Space-Time Trellis Codes

Space-time trellis codes are like single-antenna trellis codes except that memory is encoded both in time and in space. Just as single-antenna trellis codes perform significantly better than single-antenna block codes, space-time trellis codes perform significantly better than space-time block codes.

The improvement in performance comes at two costs: 1) computation, and 2) lack of flexibility. In terms of computation, space-time trellis codes are expensive because they require a Viterbi decoder. In terms of flexibility, space-time trellis codes suffer because, unlike space-time block codes, they are specific to a signal constellation.

Up until now, most of the literature has focused on designing space-time trellis codes for equal-energy (PSK) constellations and for four or less transmit antennas. A PSK trellis code has two equivalent representations: 1) as a generator matrix [17], and 2) as a trellis [10].

As explained in [17], a generator matrix G for a M-PSK code consists of n_T columns and $m + s$ rows, where $m = \log_2 M$, $s = \log_2 S$ and S is the number of states for the trellis code. Each of the coefficients in the matrix is constrained to be between 0 and M-1. For example, a 4-PSK four-state trellis code given in [10] takes the form:

$$G = \begin{pmatrix} 2 & 0 \\ 1 & 0 \\ 0 & 2 \\ 0 & 1 \end{pmatrix}$$

$m = 2$ bits are shifted in at each timestep, and with the previous $s = 2$ bits, they are used to generate $n_T = 2$ outputs mod $M = 4$. The values of the s previous bits capture the state of the trellis; these s bits are initialized to 0s. An equivalent representation of this generator matrix is the trellis shown in Figure 2-4 and given in [10]. Here it is assumed the trellis starts from the first state.

The trellis above is an example of delay diversity [18], i.e. transmit antenna 2 sends out a delayed version of the stream sent out by transmit antenna 1. The trellis code is rate 1

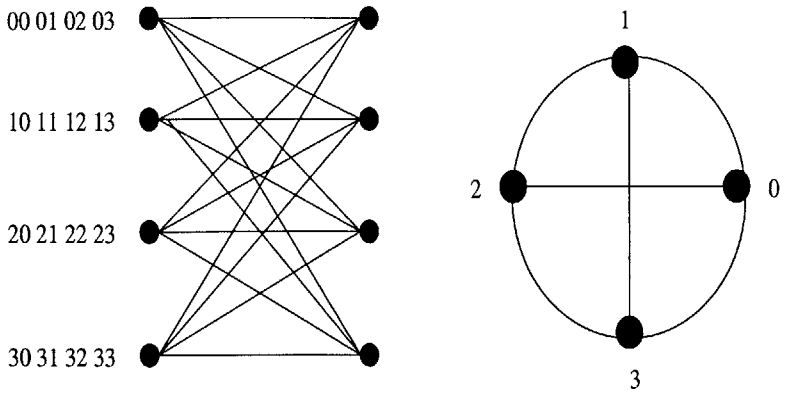

Figure 2-4: *4 state 4-PSK 2 antenna trellis code*

and achieves a diversity of 2.

In Figure 2-5, the simulated performance of the four-state 4-PSK trellis code above is plotted, along with the simulated performance of two other trellis codes. The other two trellis codes are the 8-PSK, sixteen-state trellis code given in [10] and the four-antenna, 4-PSK, 64-state trellis code given in [12]. The four-antenna trellis code is described by the generator matrix:

$$G = \begin{pmatrix} 0 & 2 & 2 & 1 \\ 2 & 2 & 0 & 2 \\ 3 & 1 & 0 & 2 \\ 2 & 2 & 2 & 0 \\ 3 & 3 & 2 & 2 \\ 0 & 0 & 3 & 1 \\ 3 & 2 & 1 & 3 \\ 2 & 0 & 1 & 2 \end{pmatrix}$$

Figure 2-5 plots the performance in terms of frame error rate, a more convenient measure for trellis codes. The SNR calculation for OSTBC codes can be used for trellis codes too, and the SNR reduces to $\frac{n_T E_s}{N_o}$. The 64-state trellis code was encoded over frames of length 256 symbols/frame, while the 8-PSK trellis code was encoded over frames of length 128 symbols/frame. Both of these trellis codes as described here were used in the Lincoln experiment.

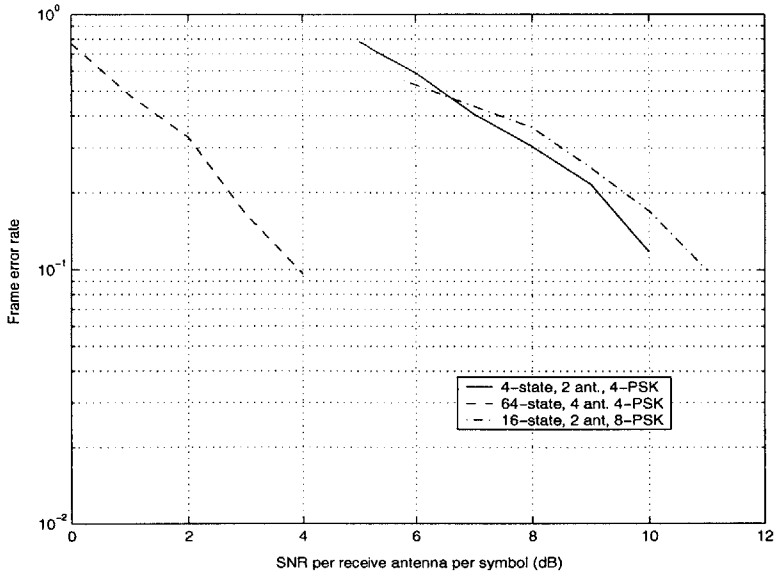

Figure 2-5: *Performance of a few trellis codes*

2.5 Space-Time Codes for the MSK Constellation

So far in this chapter the performance of space-time codes has been considered for codes constructed using criteria devised for QAM modulation. These criteria can not be directly applied to other types of modulation except in a few special cases. One of these cases is minimum shift keying (MSK) modulation, which is a type of continuous-phase modulation.

The reason the space-time codes criteria above apply to MSK modulation is that MSK modulation can be expressed as a form of QAM modulation. As shown in [19] (p. 194), an MSK signal $v(t)$ at baseband can be represented as:

$$v(t) = \sum_{n=-\infty}^{\infty} (c^{2n} g(t - 2nT) - jc^{2n+1} g(t - 2nT - T))$$

where

$$g(t) = \left\{ \begin{array}{ll} sin\frac{\pi t}{2T}, & 0 \leq t \leq 2T \\ 0, & otherwise \end{array} \right\}$$

T represents the symbol period, c^k represents the kth BPSK-modulated input symbol, and $g(t)$ is the modulated pulse shape, which corresponds to one half-cycle of a sine wave of period $2T$. The even bits are modulated on the cosine carrier and the odd bits are

modulated on the sine carrier.

The optimal receiver for MSK would use a matched-filter of the form $g^*(-t)$ and sample every T seconds. Because $g(t)$ spans $2T$ in time, the autocorrelation function of $g(t)$ spans $4T$ in time, and each symbol experiences intersymbol interference (ISI) from its two adjacent symbols. The autocorrelation of $g(t)$ is plotted in figure 2-6. The overall effect of the matched filter and sampling can be expressed as a discrete-time filter $h[n]$ with three taps, h_{-1}, h_0, and h_1. The values of these three taps can be obtained from the autocorrelation function of $g(t)$; assuming h_0 is normalized to 1, the three taps are $h_{-1} = h_1 = .3183$ and $h_0 = 1$.

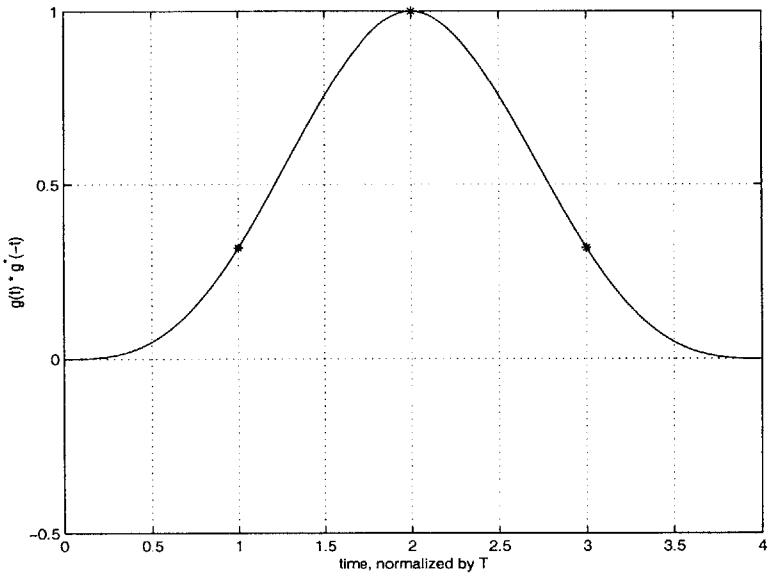

Figure 2-6: *Autocorrelation function of MSK pulse shape: stars indicates taps for the equivalent discrete-time filter*

For MSK with multiple antennas, the difference matrix $B(C,E)$, can be expressed as the product of three matrices: one which equals $C - E$, a second diagonal matrix J which accounts for the even/odd input symbol multiplication by 1 or $-j$, respectively, and a third Toeplitz matrix H which accounts for the effect of the discrete-time filter $h[n]$.

$$B(C,E) = \begin{pmatrix} c_1^1 - e_1^1 & c_1^2 - e_1^2 & \dots & c_1^l - e_1^1 \\ c_2^1 - e_2^1 & c_2^2 - e_2^2 & \dots & c_2^l - e_2^l \\ \vdots & \vdots & \ddots & \vdots \\ c_{n_T}^1 - e_{n_T}^1 & c_{n_T}^2 - e_{n_T}^2 & \dots & c_{n_T}^l - e_{n_T}^l \end{pmatrix} \begin{pmatrix} 1 & 0 & \dots & 0 \\ 0 & -j & \dots & 0 \\ \vdots & \vdots & \ddots & \vdots \end{pmatrix} \begin{pmatrix} h_0 & h_{-1} & 0 & \dots & 0 \\ h_1 & h_0 & h_{-1} & \dots & 0 \\ \vdots & \vdots & & \ddots & \vdots \\ 0 & 0 & 0 & \dots & h_0 \end{pmatrix}$$

The space-time code criteria derived above are unaffected by the presence of the matrices J and H. The argument can be made more explicit by doing a singular value decomposition of each of the three matrices.

The argument can be extended to any form of QAM modulation which intentionally introduces ISI for spectral efficiency. For example, as [20] shows, Gaussian Minimum Shift Keying can be well approximated as a form of PAM modulation, and thus the space-time codes criteria devised above also apply in that case.

A more extended discussion of space-time coding for continuous phase modulation can be found in [21].

Chapter 3

The Lincoln Experiment Setup

In the last chapter simulation results were presented for the experiments relevant to this thesis that were carried out with Lincoln Labs. Here, more detailed specifications for carrying out those experiments are presented. In particular, this chapter focuses on the field test hardware setup, the type of experiments carried out and what data is transmitted, and how channel estimation is performed.

3.1 The Hardware Setup

Much of the hardware infrastructure for this experiment was available from previous experiments at Lincoln Labs [1], [22]. The Lincoln indoor field test setup had the capacity to test scenarios with up to 8 transmit antennas and 10 receive antennas. The transmit and receive antennas were stationary, so the quasi-static fading model, excluding the assumption of ideal CSI, is a fairly realistic approximation. Transmissions from the 8 transmit antennas were synchronized by equipping the transmit boxes with GPS receivers that read in a common GPS signal.

The transmit antennas operated at a carrier frequency of 1790 MHz; this carrier frequency was provided to all transmit boxes by a common 1790 MHz oscillator crystal. Because the crystal frequency was supposed to be accurate to 10^{-6}, a common carrier frequency offset on the order of 2 kHz could be expected. In reality, an offset of about 8 kHz was observed, and this offset was compensated for by a shift in the intermediate frequency at the receiver. An amplifier was used at the output of the oscillator to provide a signal strong enough to support all 8 transmit antennas.

Data files containing samples to be transmitted were loaded onto the hard drives of all 8 transmit antenna boxes. The data represented samples at 2×1.2288 complex megasamples/s. A symbol frequency of 122.88 complex kilosamples/s was chosen for convenience so that each symbol period could correspond to an integer number of samples per symbol (20 samples/symbol). The (doubled-sided) bandwidth of the system was set to 165.88 kHz, and a root raised cosine waveform of 121 samples, roughly six symbol periods, was used for pulse shaping at the transmitter. (Chapter IV covers the process of choosing the right pulse shape in more detail.)

The function of the receiver, consisting of ten channels, was to bring down the received signal to an intermediate frequency of 5 MHz and store samples of the signal at the intermediate frequency at a sampling rate of 2×1.2288 complex megasamples/s. The table below summarizes the key parameters for the Lincoln indoor field test hardware setup.

Parameter	Value
max n_T	8
n_R	10
symbol rate	122.88 kHz
bandwidth	165.88 kHz
carrier frequency	1790 MHz
transmitter sampling frequency	2×1.2288 complex megsamples/s
receiver sampling frequency	2×1.2288 complex megasamples/s

3.2 The Field Test

The indoor field test at Lincoln Labs took place in mid June, and sixteen significantly different space-time coding scenarios were tested. These scenarios were chosen to test a range of space-time codes, including low density parity check space-time codes, space time codes for CDMA, space-time turbo codes, space-time block codes, and space-time trellis codes, for both four and eight transmit antennas. Some scenarios with eight transmit antennas were designed to have two groups of four transmit antennas that functioned as competing MIMO interferers.

A few of the scenarios based on block and trellis codes are listed in the table below. Some of the scenarios with four or less transmit antennas were combined with other scenarios

with four or less transmit antennas so that interference suppression decoding [23] could be performed.

Scenario	n_T	n_R	$\mathcal{S}$	ST Code	ρ
1	1	10	4-PSK	uncoded	2
2	2	10	4-PSK	Alamouti	2
3	2	10	8-PSK	16-state trellis	3
4	4	10	16-QAM	rate $\frac{3}{4}$ block	3
5	4	10	4-PSK	64-state trellis	2
6	8	10	64-QAM	rate $\frac{1}{2}$ block	3

The last column ρ specifies the spectral efficiency in bits/sec/Hz. The simulated performance of all of these scenarios was presented in the previous chapter.

For this thesis, only the performances of scenario 1 and scenario 2 are analyzed and compared. Figure 3-1 - 3-2 make it more clear what is exactly going on for each of the two scenarios.

There are a few things in common with all or most of the scenarios listed in the above table. First, all schemes use Gray-labeled signal constellations. Second, the data stream used for all scenarios is a common maximal-length pseudonoise (PN) sequence generated by a 16-stage linear feedback shift register (LFSR). Maximal length sequences are known to have excellent autocorrelation properties (i.e. are close to random), and repeat themselves every $2^m - 1$ iterations through the shift register, where m is the number of stages in the LFSR. The data stream was generated with the generator polynomial $x^{16} + x^{12} + x^3 + x^2 + 1$, and the shift register was initialized to all ones. And third, for most scenarios, the data is additionally convolutionally encoded with a constraint-length 7, rate $\frac{1}{2}$, (171, 133) convolutional code before channel encoding. Note that forward error correction coding has been completely separated from channel coding; in chapter 2 ([7], [8]) it was argued that such an arrangement promotes modularity while giving good BER performance.

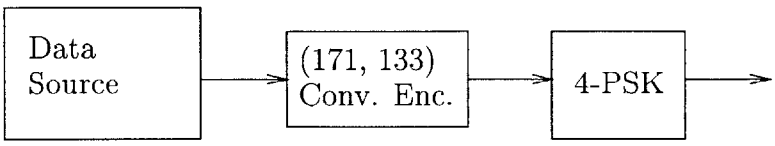

Figure 3-1: *Scenario 1: 4-PSK, uncoded, SISO*

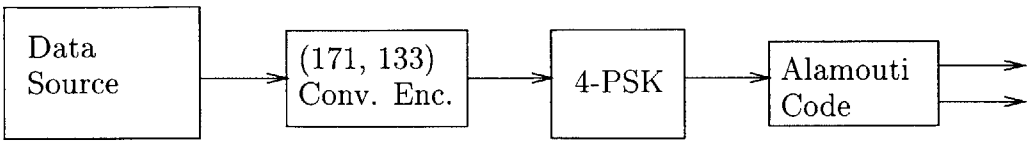

Figure 3-2: *Scenario 2: 4-PSK, Alamouti code*

3.3 Transmission Burst Structure

As stated before, the transmitter synchronized bursts using a common GPS signal read in by the GPS receivers on each transmit box. Each burst was designed to last approximately 1.7 seconds long and was associated with a specific space-time code. Within the 1.7 seconds, 1.5 seconds was devoted to transmitting the associated space-time code and the rest of the time was taken up mostly by channel estimation sequences.

Figure 3-3 shows the structure of each burst in more detail. The burst structure is shown as it was designed for eight transmit antennas. With four or less transmit antennas the transmission burst structure is exactly the same with some antennas simply turned off. Each burst consists of four main components: the tones, the noise estimate, the channel estimate sequences (for single and multiple antennas), and the space-time-encoded data. In addition, there is, not shown in the figure, some filler space between each segment on the order of 100 samples.

The tones were sent jointly from eight transmit antennas at frequencies of 20 kHz, -40 kHz, 60 kHz, -80 kHz, 100 kHz, -120 kHz, 140 kHz, and -160 kHz. Since the waveform from each transmit antenna is orthogonal to the waveforms from other transmit antennas, separating these tones at the receiver can be easily accomplished. The purpose of the tones is to provide a simple characterization of the channel response at different frequencies. In addition, the tones show the extent the carrier frequency deviates from 1790 MHz due to oscillator error.

During the noise estimation portion of the transmission burst, the transmit antennas were simply turned off, i.e. nothing was transmitted, and whatever the receiver registered was counted as noise. The purpose of this portion was to enable understanding the system noise characteristics.

The single and joint antenna channel estimation sequences characterized the channel coefficients from each transmit antenna to each receive antenna. These estimates provided

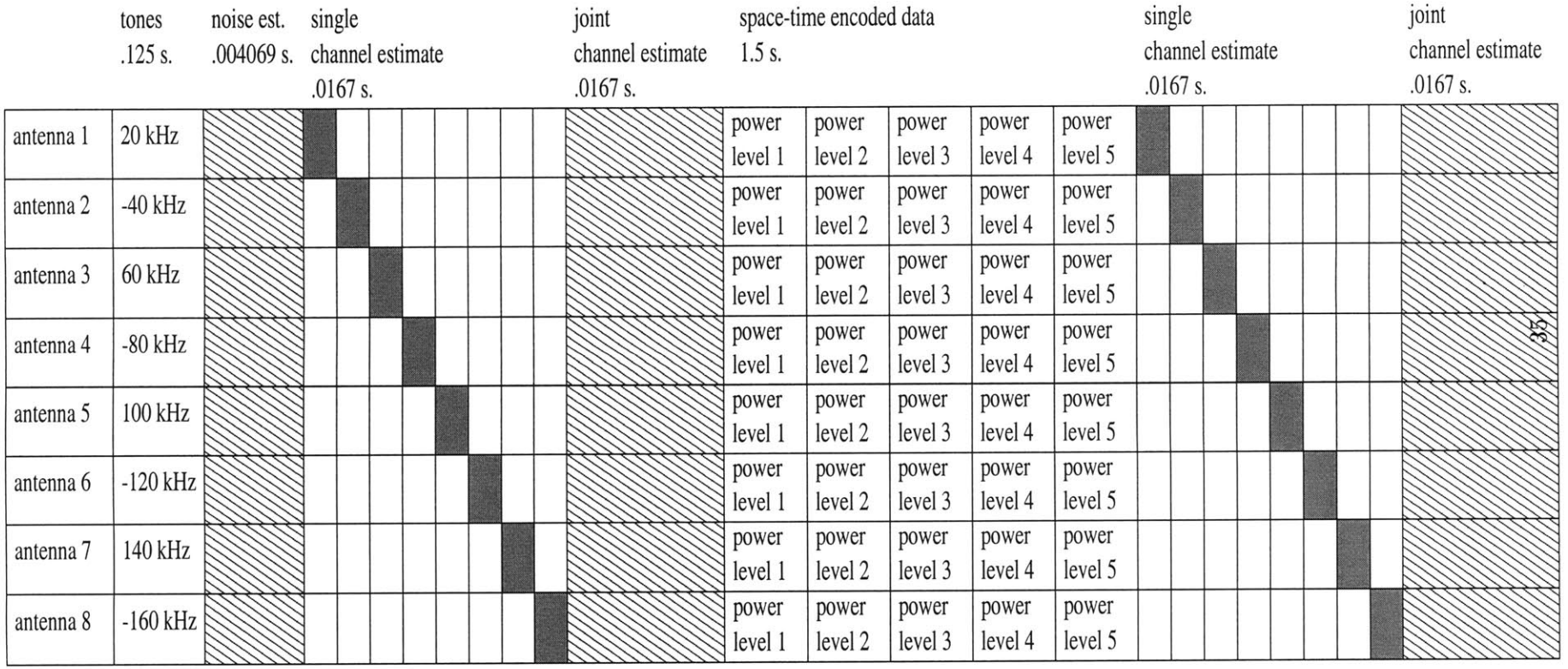

Figure 3-3: *Structure of Transmission Burst*

by these sequences weren't actually used for decoding the space-time encoded data but were used to give a picture of how the channel varied over time; thus it wasn't important to restrict the bandwidth of the channel probing sequences to the same bandwidth that the pulse-shaping filter was restricted to at the modulator (165.888 kHz). The single antenna channel estimation sequences captured the channel coefficient from a specific transmit antenna to a specific receive antenna. The joint antenna channel estimation sequences allowed for analyzing the correlation between transmit antennas.

The space-time-encoded data segment, which lasted 1.5 s., was split into 5 portions of .3 seconds each. Each portion corresponded to a specific power level, and the power was stepped down 3 dBs at a time between portions. The purpose of using different power levels was to gain an idea of how the space-time codes performed over a range of SNR values. For each of the scenarios, two transmission bursts were sent to test two regimes of SNR values, high SNR and normal SNR.

3.4 Channel Estimation Sequences

The work here on channel estimation is due to Dr. Ali Yegulalp at Lincoln Labs [24]. For estimating the channel between a single transmit antenna and the receive antennas, he used a waveform $z(t)$ that was essentially a periodic chirp; the functional form of the waveform at baseband in continuous time is:

$$z(t) = e^{j\frac{WM}{2}\sin(\frac{2\pi t}{T})}$$

(In reality, the function stored on the hard drive of the transmit antenna box represents discrete-time samples at the transmitter sampling frequency 2×1.2288 complex megasamples/s.) W equals the double-sided bandwidth to be probed, and M is the period of the waveform. Because the sine wave in the phase is periodic with period M, $z(t)$ is also periodic with period M.

$z(t)$, in addition to being a good channel estimation sequence in the minimum mean-squared sense, has two other desirable properties:

- $z(t)$ is constant modulus, i.e. the function is smooth and doesn't change too rapidly or abruptly from one time instant to the next. The constant modulus property, which

doesn't hold for channel estimation sequences based on PN sequences, prevents the probing of transmitter non-linearities.

- Unlike other types of chirps, $z(t)$ is essentially band-limited to the range $\frac{-W}{2}$ to $\frac{W}{2}$. A lowpass filter that may degrade performance is not necessary for $z(t)$.

Because $z(t)$ is periodic with period M, the spectrum of z(t) is non-zero only at discrete multiples of the fundamental frequency $\frac{1}{M}$. It can be shown that the magnitude of the spectrum at the kth multiple of $\frac{1}{M}$ is given by:

$$s_k = J_k(\frac{WM}{2})$$

where $J_k()$ represents the Bessel function of the first kind. Figure 3-4 plots the Bode plot of the magnitude of the spectrum of $z(t)$ sampled at the transmitter sampling frequency with W and $\frac{1}{M}$ set to $\frac{3}{5} \times 2 \times 1.2288$ MHz and $\frac{1}{512} \times 2 \times 1.2288$ MHz, respectively. The channel probing sequence used for the Lincoln experiment used the same parameter values. Outside the range [-$\frac{W}{2}$: $\frac{W}{2}$], it can be shown that the spectrum decays exponentially.

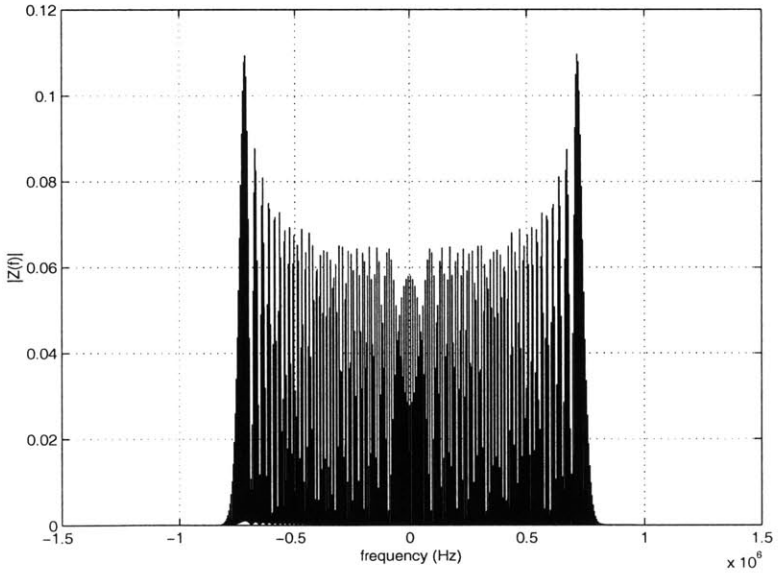

Figure 3-4: *The magnitude of the spectrum of z(t), the single-antenna channel estimation sequence*

To perform channel estimation at any specific receive antenna, first a lowpass filter is applied to the received signal around the bandwidth of interest, [-82.944 82.944] kHz. Because the system is narrowband, i.e. there is flat fading, the lowpass-filtered signal can

then be matched filtered and sampled to find the appropriate subchannel tap. If the noise is white, the matched filter and sampling operation are optimal in the minimum mean squared sense [27].

3.4.1 Joint Antenna Channel Estimation

Joint antenna channel estimation can be easily accomplished by slightly modifying the above waveform for each transmit antenna. In particular, it can be shown that if a waveform $s(t)$ is periodic with period M, then the collection of waveforms $s(t)e^{j\frac{2\pi kt}{NM}}$, with $0 \leq k < N$ and k discrete, forms an orthogonal set. The orthogonality can be seen from the transform domain where it is apparent that any two different waveforms in the set are never non-zero at the same frequency.

The solution for joint antenna channel estimation is for each transmit antenna to send a different waveform in the set. For eight transmit antennas, N was set to 8 to obtain eight waveforms, and transmit antenna i sent the waveform $s(t)e^{j\frac{2\pi it}{NM}}$.

At any specific receive antenna, the spectrum of the received signal $r(t)$ is the sum of the spectra for each of the eight transmitted waveforms modified by the appropriate subchannel coefficients. Because the signals are orthogonal, channel estimation for the joint transmit case can be achieved in a manner analogous to the way estimation is achieved for the single transmit case: first a lowpass filter is applied; then the signal is matched-filtered and sampled.

Chapter 4

Pulse Shaping Design and the Receiver Front-End

In the previous chapters, a discrete-time model was considered in the analysis of performance for different transmission and reception scenarios. While sufficient and elegant for analysis, this model hides the details of transmitting signals over a continuous-time band-limited channel. These details include, for instance, the application of a pulse shaping filter at the modulator to constrain the transmitted signal spectrum and the use of a whitening matched filter (WMF) at the front-end of the receiver. In this chapter the design of these lower-level elements that contribute to the discrete-time model abstraction are investigated in the context of the experiments at Lincoln. As in chapter II, the ideal channel model presented in chapter I is assumed.

A brief summary of the results of the design process are as follows: A root raised cosine filter with a rolloff of .35 was chosen for shaping at the modulator. The root raised cosine filter, in addition to limiting the bandwidth of the transmitted pulse, is desirable because it satisfies the Nyquist criterion for no intersymbol interference (ISI). At the receiver, the matched filter was designed to accommodate processing for a variable number of samples per symbol. A whitening filter was unnecessary because of the zero-ISI property of the raised cosine pulse.

4.1 Derivation of the Discrete-Time Model

In this section the discrete-time model is derived specifically for the MIMO system used in the Lincoln experiment. The derivation closely parallels the derivation of the discrete-time model for the SISO AWGN system in [19, p. 548-561].

4.1.1 The Transmitter

Figure 4-1 illustrates the system in the Lincoln experiment between the output of the channel encoder at the transmit antennas and the input to the MIMO channel. n_T denotes the total number of transmit antennas, which are assumed to be synchronized. It is important to note that all operations up to and including the discrete-time matched filter were done offline for the Lincoln experiment; only the D/A conversion and modulation were done in real-time.

At the output of the channel encoder, each transmit antenna i has a sequence of symbols c_i^k, $0 \leq k \leq \infty$ it wishes to transmit and which are members of a complex constellation $\mathcal{S}$. For the Lincoln experiment, the constellation was either 4-PSK, 8-PSK, 16-QAM, or 64-QAM. This sequence of symbols can be considered to arise from a process being sampled at $1/L$ complex samples/s. $1/L$ is the rate the transmit antenna expects samples before they are converted from digital to analog; in the Lincoln experiment this rate is fixed to $2 \times 1.2288 \times 10^6$ samples/s.

The purpose of the upsampler at each transmit antenna is to bring down the rate of the symbols from the sampling rate required by the transmit antenna to the symbol rate

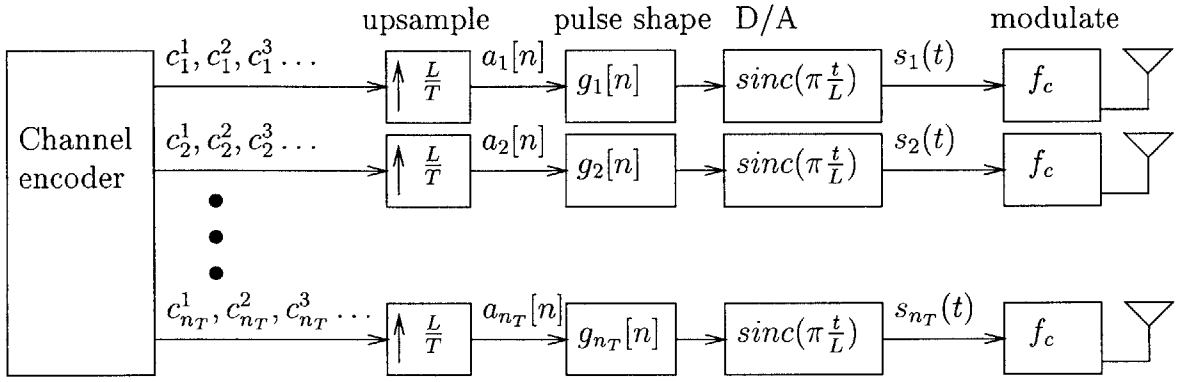

Figure 4-1: *The Transmitter*

desired for the system. The symbol rate is represented as $1/T$; for the Lincoln experiment $1/T$ was set to 122.88×10^3 symbols/s; this choice was convenient because each symbol duration then corresponds to exactly 20 samples (having an integer number of samples per symbol makes everything easier to deal with). The signal in its lowpass representation out of the upsampler for each antenna takes the form:

$$a_i[n] = \sum_{k=0}^{+\infty} c_i^k \delta[n - k\frac{L}{T}]$$

The signal at the output of the upsampler has infinite bandwidth. In order to make it suitable for transmission over a bandlimited channel, a discrete-time pulse shaping filter $g_i[n]$ must be applied. $g_i[n]$ is a filter which represents samples at a sampling rate of $1/L$ of the continuous-time pulse-shaping filter $g_i(t)$ that will come about as a result of the D/A at each transmit antenna. $g_i(t)$, and correspondingly $g_i[n]$, must be chosen so that they meet the system bandwidth constraint system: if B corresponds to the single-sided lowpass bandwidth limit for the Lincoln system, then it must be true that the Fourier transform $G_i(f)$ of $g_i(t)$ satisfies $G_i(f) = 0$ for $|f| \geq B$. In addition, $g_i(t)$ should have its total energy normalized to 1. Later the process of choosing the pulse $g_i(t)$ is discussed.

(Note that in an optimized system, it may be more convenient to switch the order of the upsampling block and the pulse shaping block in order to gain in terms of computation.)

After the pulse-shaping block, each transmit antenna performs a D/A conversion which can be represented as an ideal interpolating filter of the form $sinc(\frac{\pi}{L}t)$, where $sinc(x) = \frac{\sin(x)}{x}$. The resulting signal is:

$$s_i(t) = \sum_{k=0}^{+\infty} c_i^k g_i(t - kT)$$

The last step at the transmitter is to modulate $s_i(t)$ onto a carrier of frequency $f_c \gg B$. For the Lincoln system, $f_c = 1790$ MHz.

4.1.2 The Front-End of the Receiver

Figure 4-2 illustrates the front-end of the receiver for a MIMO system with n_T transmit antennas and n_R receive antennas. Each receive antenna j gets a linear combination of the signals from each transmit antenna i, plus some zero-mean AWGN $n_j(t)$. The linear

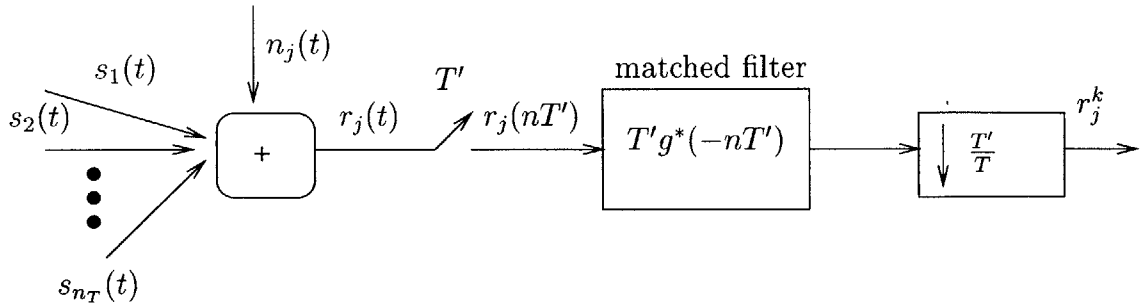

Figure 4-2: *The Receiver Front-End*

combination is specified by the channel matrix H, which as discussed in chapter 1, is of the form:

$$H = \begin{pmatrix} \alpha_{1,1} & \alpha_{2,1} & \cdots & \alpha_{n_T,1} \\ \alpha_{1,2} & \alpha_{2,2} & \cdots & \alpha_{n_T,2} \\ \vdots & \vdots & \ddots & \vdots \\ \alpha_{1,n_R} & \alpha_{2,n_R} & \cdots & \alpha_{n_T,n_R} \end{pmatrix}$$

Each coefficient in the H matrix is a Rayleigh random variable. We assume that the received signal has been brought down to baseband and that it has been lowpass filtered around the $[-B, B]$ band to reject out-of-band noise. (In terms of actual implementation, the matched filter serves as the lowpass filter.) Also, it is important to note that all reception for the Lincoln experiment after the initial sampling was performed offline.

In its lowpass form, the noise $n_j(t)$ has the power density spectrum shown in Figure 4-3(a); the variance of $n_j(t)$ equals $N_o B$ per real dimension. The received signal at each receive antenna can be expressed as:

$$r_j(t) = \sum_{k=0}^{\infty} \sum_{i=1}^{n_T} \alpha_{i,j} c_i^k g_i(t - kT) + n_j(t)$$

The next step is to sample the received signal at each antenna at a rate $1/T'$. This step differs from the model for SISO channels in that the matched filtering now must take place in discrete-time rather than in continuous-time. $1/T'$ is chosen to be at least twice the symbol rate $1/T$. For a practical system $1/T'$ might equal $4/T$ or $8/T$, so that the receiver can do processing on 4 or 8 samples per symbol. For the sake of simplicity it is assumed that $1/T'$ is an integer multiple of $1/T$, so that the received signal after the initial sampling

can be written as:

$$r_j[n] = \sum_{k=0}^{\infty} \sum_{i=1}^{n_T} \alpha_{i,j} c_i^k g_i((n - k\frac{T}{T'})T') + n_j(nT')$$

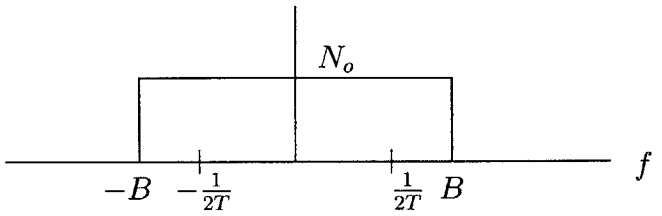

(a) Upon reception

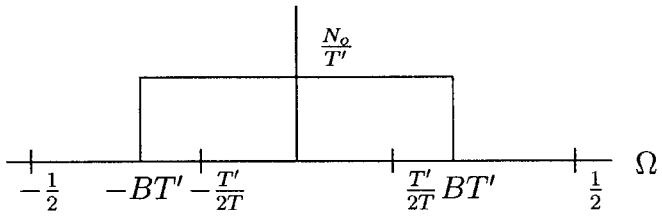

(b) After first sampling

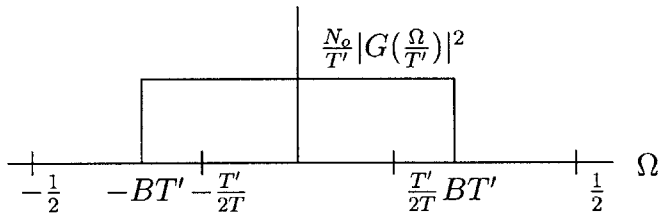

(c) After matched filter

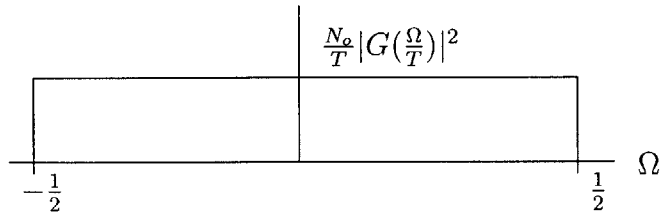

(d) After decimation

Figure 4-3: *Evolution of noise p.s.d. at receiver front end*

The effect of the sampling on the noise p.s.d. is illustrated in Figure 4-3(b).

How reception is handled from here depends on the choice of the pulse shape $g_i(t)$. For simplicity, $g_i(t)$ is assumed to be is the same across all transmit antennas and is equal

to a global pulse shape $g(t)$. Let $G(f)$ denote the Fourier transform of $g(t)$. Under this assumption, the front-end receiver for the MIMO channel (besides the initial sampling) reduces to the textbook case for SISO AWGN channels. In particular, by letting $\sum_{i=1}^{n_T} \alpha_{i,j} c_i^k$ be equivalent to a symbol that is sent from a transmitter in the SISO AWGN channel case, the optimal front end receiver becomes a discrete-time matched filter of the form $T' g^*(-nT')$. The scaling by a factor of T' is necessary in order to get the same effect on the p.s.d as one would want if the matched filter were implemented in continuous-time.

The next step is to decimate by a factor of T'/T so that now all processing can be done at the symbol rate $1/T$. The decimation causes the noise p.s.d. to change as depicted in Figure 4-3(d). It is observed from these figures that, with an appropriate choice of the pulse shape $g(t)$, the noise p.s.d. can be made white and intersymbol interference can be eliminated. In particular, the choice of the pulse shape should satisfy Nyquist's criterion for no ISI, i.e.

$$\sum_{k=-\infty}^{\infty} |G(f - \frac{k}{T})|^2 = T$$

This criterion can be satisfied if $1/T \leq 2B$, a constraint that is met for the Lincoln experiment. If the chosen pulse shape satisfies Nyquist's criterion, then the resulting discrete time model can be expressed as:

$$r_j^k = \sum_{i=1}^{n_T} \alpha_{i,j} c_i^k + n_j^k$$

n_j^k corresponds to zero-mean white Gaussian noise of variance $N_o/2$ per real dimension.

4.2 Pulse Shaping Design

4.2.1 Root Raised Cosine Pulse Description

One of the most commonly used pulse shapes designed to eliminate ISI for a QAM system is the root raised cosine. The root raised cosine, designed for a symbol rate $1/T$, is a real symmetric pulse with power spectral density given by [19, p. 561]:

$$|P(f)|^2 = \begin{pmatrix} T & 0 \le |f| \le \frac{1-\beta}{2T} \\ \frac{T}{2}(1 + cos(\frac{\pi T}{\beta}(|f| - \frac{1-\beta}{2T}))) & \frac{1-B}{2T} \le |f| \le \frac{1+B}{2T} \\ 0 & |f| > \frac{1+\beta}{2T} \end{pmatrix}$$

The parameter β is known as the rolloff factor and determines how much excess bandwidth beyond the minimum bandwidth $\frac{1}{2T}$ is necessary to transmit with no ISI. The rolloff factor is constrained to be between 0 and 1. If $\beta = 0$, then no excess bandwidth is being used, and $|P(f)|^2$ corresponds to the ideal brick wall spectrum. If $\beta = 1$, then $|P(f)|^2$ uses 100 percent excess bandwidth. Figure 4-4 plots $|P(f)|^2$ for different values of β.

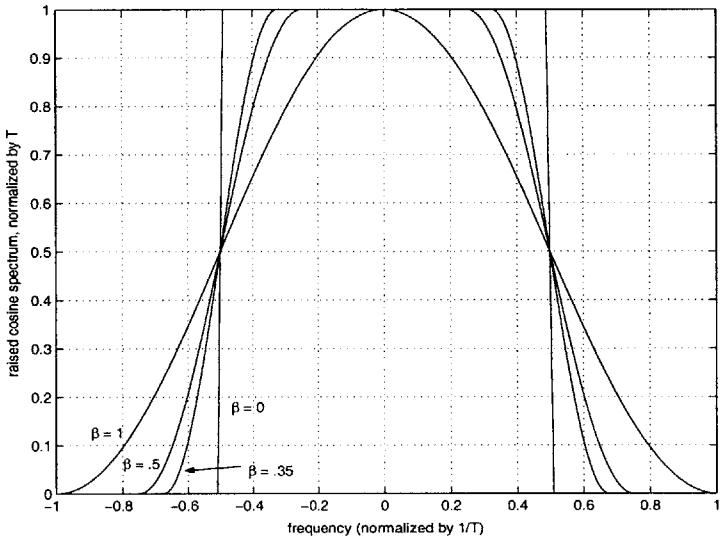

Figure 4-4: *Raised cosine pulse in the frequency domain for different rolloff values*

The p.s.d. of the root raised cosine corresponds to the Fourier transform of the deterministic autocorrelation of the root raised cosine. This autocorrelation function, known as a raised cosine pulse, can be determined by taking the inverse Fourier transform of the spectrum above to yield:

$$p(t) * p^*(-t) = sinc(\pi \frac{t}{T}) \frac{cos(\pi \beta t/T)}{1 - 4\beta^2 t^2/T^2}$$

The raised cosine function in the time domain is plotted in Figure 4-5 for different values of β. The zero-ISI property of the pulse is apparent in the fact the pulse goes to 0

at multiples of T. As β approaches 0, the pulse converges to the *sinc* function.

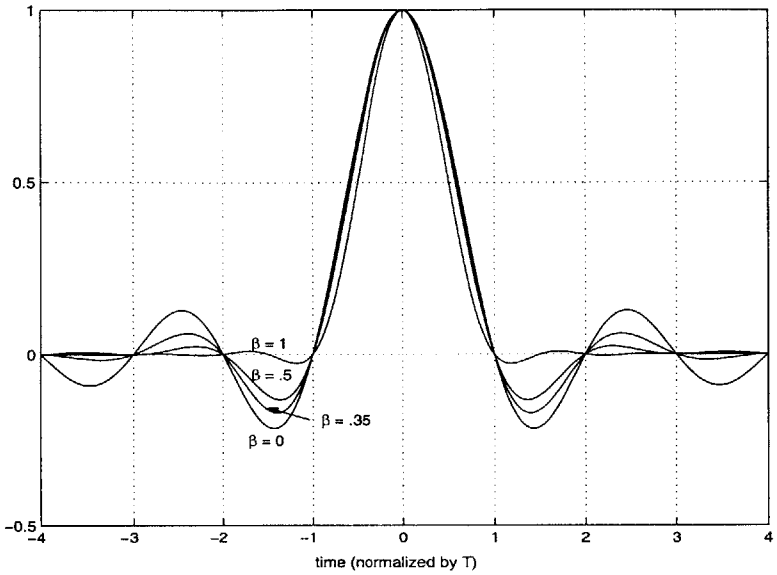

Figure 4-5: *Raised cosine pulse in the time domain with different rolloff values*

The root raised cosine pulse can be determined analytically by taking the inverse Fourier transform of the square root of the p.s.d. show above. The pulse is [25]:

$$p(t) = \frac{4\beta}{\pi\sqrt{T}} \frac{cos((1+\beta)\pi\frac{t}{T}) + \frac{sin((1-\beta)\pi\frac{t}{T})}{4\beta\frac{t}{T}}}{1-(4\beta\frac{t}{T})^2}$$

4.2.2 Root Raised Cosine Pulses in Practice

For $p(t)$ to be used in practice, two more design issues have to be dealt with: 1) an appropriate value for β must be chosen, and 2) because the root raised cosine pulse is not time-limited, an appropriate time-domain window must be chosen.

Setting β

Choosing a good value for β and an appropriate window involve several tradeoffs. First, the ideal is to use $\beta = 0$; this value of β, which yields a *sinc* function, maximizes bandwidth efficiency under the constraint that there is no ISI. The problem with using a *sinc* function in practice, however, is that it is vulnerable to sampling uncertainties at the output of the matched filter at the receiver: because the tails of the *sinc* decay only as $1/t$ over time, missampling by even the slightest margin will introduce massive amounts of ISI.

In the end β was set to .35. This value of β corresponds to having a double-sided bandwidth of 165.888×10^3 Hz, i.e. $B = 82.944 \times 10^3 Hz$. This value of β provided a good engineering balance. In general, it was desirable to keep the amount of bandwidth in the range of $150 - 170$ kHz, and $\beta = .35$ also seems to have been a popular choice in many other practical systems. This value for β yields reasonable bandwidth efficiency while avoiding the timing uncertainties inherent in using a lower value.

Choosing a window

The type of window that is applied to the root raised cosine pulse also involves several tradeoffs. There are two issues here that are related: the length of the window, and the amount of window taper. Setting the window length parameter involves a tradeoff between the amount of computation vs. the amount of ISI at the output of the matched filter at the receiver. As the window length grows longer, the ISI is reduced because the root raised cosine pulse becomes less and less distorted; at the same time, computation throughout the system is increased.

Choosing the amount of taper in the window involves a tradeoff between the amount of ISI at the receiver and the amount of energy transmitted outside the band $[-B : B]$. If the window were rectangular, i.e. had no taper, the resulting pulse would minimize the amount of ISI at the receiver; however, at the same time, using a window with little or no taper will incidentally introduce undesirable ripples in the frequency domain outside of the band $[-B : B]$, and these ripples will decay in energy very slowly over the duration of the frequency spectrum.

Upon examination of a dozen common windows, including the Hamming, Blackman, Chebyshev, and Gaussian windows, a Tukey window was chosen to test the tradeoff between ISI and bandwidth leakage. The Tukey window is attractive because it is parameterized by a variable α, $0 \leq \alpha \leq 1$, that controls this very tradeoff. The equation for computing the N-point Tukey window $w[k]$ is [26]:

$$w[k+1] = \begin{pmatrix} 1.0 & 0 \leq |k| \leq \frac{N}{2}(1+\alpha) \\ .5(1 + cos(\pi \frac{k - \frac{N}{2}(1+\alpha)}{N(1-\alpha)})) & \frac{N}{2}(1+\alpha) \leq |k| \leq N \end{pmatrix}$$

The Tukey window for N=121 with different values of α is plotted in Figure 4-6. It is observed that when $\alpha = 0$, the Tukey window reduces to a rectangular window, and when

$\alpha = 1$, the Tukey window becomes a Hanning window.

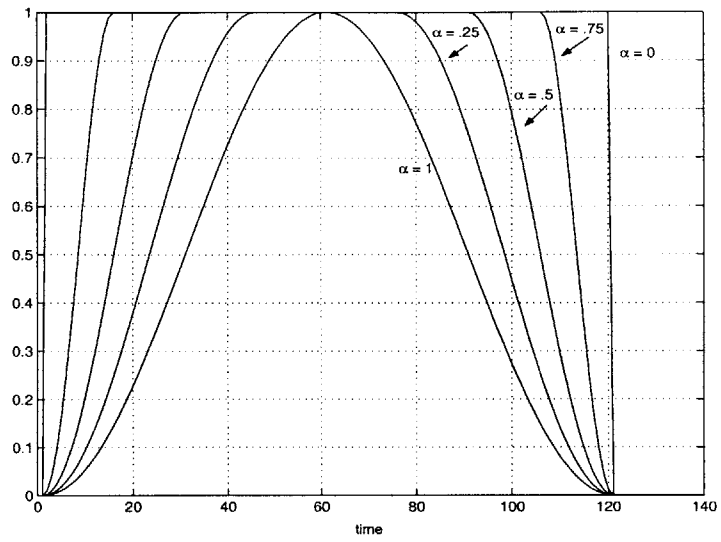

Figure 4-6: *121-point Tukey windows for different values of* α

So the solution to selecting the right window simply involves adjusting the value of α and picking an appropriate window length. In addition to adjusting α and the window-length, it was discovered that even more precise fine-tuning can be achieved by applying multiple Tukey windows in succession on the root raised cosine pulse. Thus the final choice of a window was not one window but actually three applied in a row: two Tukey windows with $\alpha = .15$ and one window equal to $\alpha = .35$. The length of all three windows was 121 samples, or approximately six symbol periods. The chosen window is shown in Figure 4-7.

4.3 Performance of the Continuous-time Model

A pulse shape $g(t)$ has been specified that is to used at each of the transmit antennas at the transmitter. This pulse shape is a 121-point windowed root raised cosine pulse with a rolloff of $\beta = .35$. The pulse was windowed with three Tukey windows, two of which had the taper parameter $\alpha = .15$ and the other of which had $\alpha = 0$. From Figure 4-1, it is seen that the discrete-time pulse to be used at the transmitter should be of the form $g(nL)$. The discrete-time matched filter at the receiver is of the form $T'g^*(-nT') = T'g(nT')$, because the chosen pulse is real and symmetric.

The resulting pulse shape gives good performance in terms of computation, bandwidth,

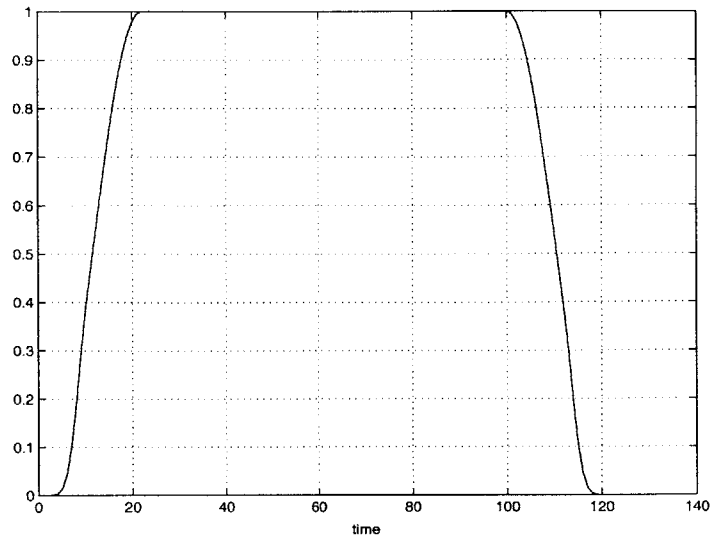

Figure 4-7: *Chosen 121-point Tukey window for windowing root raised cosine pulse*

and ISI. In terms of computation, the chosen pulse is reasonable because 121 taps is not too burdensome on the real-time transmitters. In terms of ISI, insight can be gained by looking at the pulse's autocorrelation function, plotted in Figure 4-8. The maximum ISI, assuming no channel smearing, can be calculated by comparing the sum of the absolute values of the autocorrelation function at times which are multiples of the sampling interval and not equal to 0 with the absolute value of the autocorrelation function at 0. For the chosen pulse, this value is:

$$maxISI = \frac{2\sum_{k=1}^{6} |g(k\frac{L}{T}) * g(k\frac{L}{T})|}{|g(0) * g(0)| + 2\sum_{k=1}^{6} |g(k\frac{L}{T}) * g(k\frac{L}{T})|} = .0254$$

This value means that for any given symbol, with no channel smearing, no more than 2.54 percent interference from other symbols can be expected at the sampling instant. This value is small enough that almost no loss in performance should result from using the chosen pulse shaping filter. Simulation results comparing performance between the discrete-time model and the continuous-time model for the 64 QAM SISO case bear out this conclusion: see Figure 4-9. Figure 4-10 shows roughly the amount of interference from other symbols over all points on the 64-QAM constellation at the output of the matched filter, assuming no noise in the channel. The rotation and stretching/shrinking of the constellation is due to the channel coefficient's phase and magnitude, respectively.

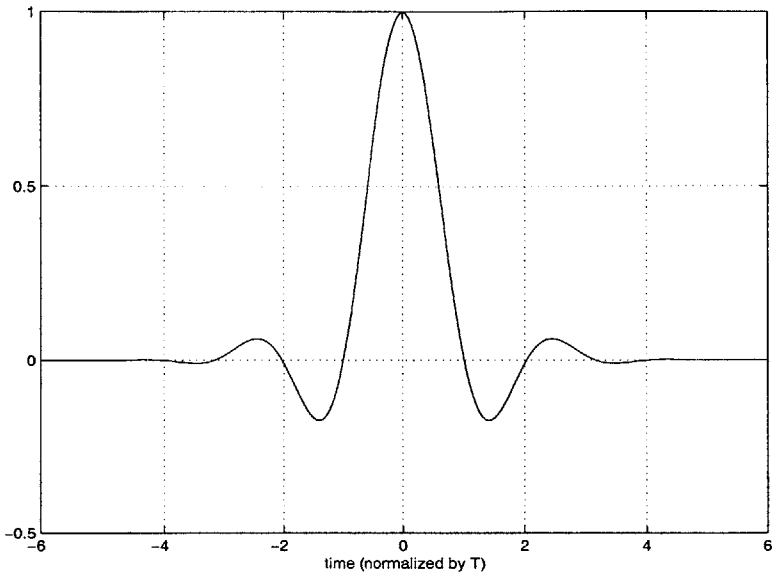

Figure 4-8: *Autocorrelation of chosen pulse g(t)*

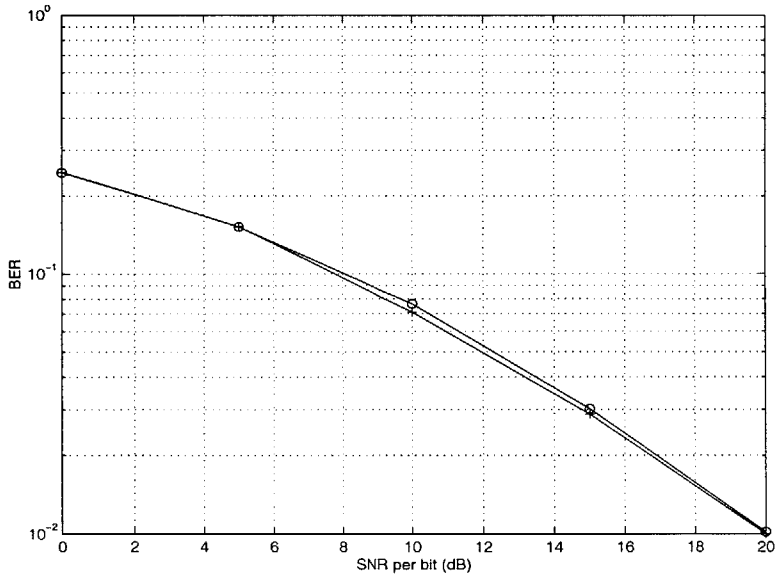

Figure 4-9: *64-QAM, SISO comparison between discrete-time model and continuous-time model*

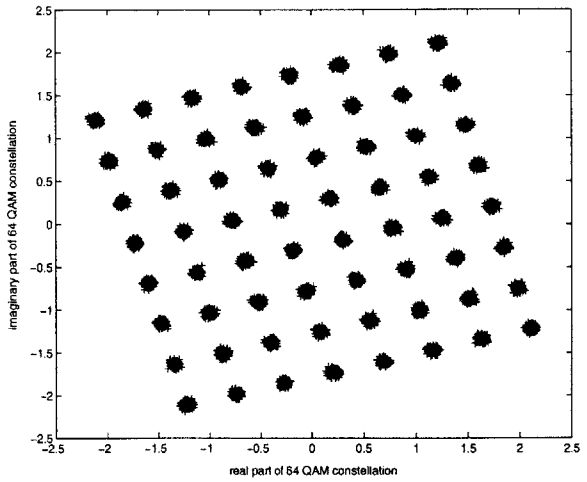

Figure 4-10: *Sample effect of channel and ISI on 64-QAM constellation*

Finally, it can be seen that the pulse meets the bandwidth requirements of the Lincoln system by looking at the spectrum plotted in Figure 4-11. At about $f = \frac{B}{2} = 82.944$ kHz, the spectrum is down about 30 dBs in power, and it continues falling outside of the system bandwidth.

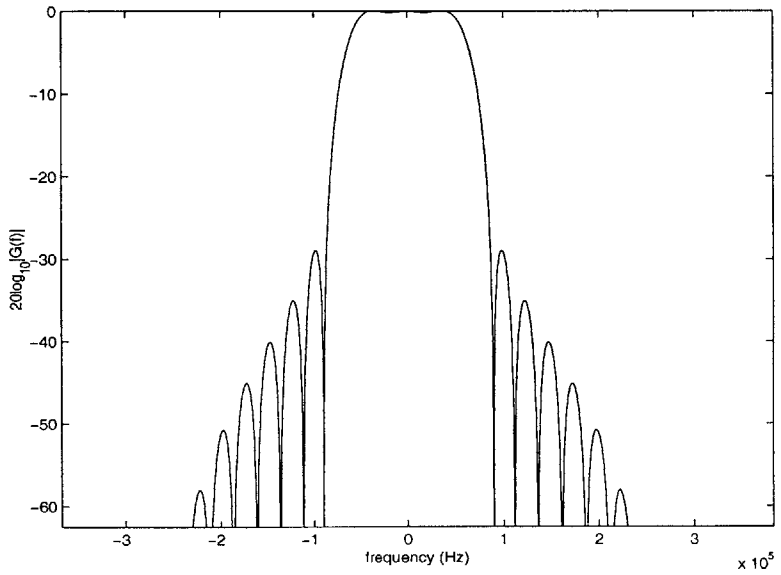

Figure 4-11: *Bode magnitude plot of the chosen pulse g(t)*

Chapter 5

Experimental Analysis

In this chapter experimental results of the indoor field test at Lincoln Labs are presented for the three scenarios described in Chapter III. This chapter begins with an analysis of the nature of the experimental channel and comparison of it to the ideal channel model presented in Chapter I. The experimental channel is analyzed by looking at the portion of the transmission burst devoted to the tones, noise, and channel estimation sequences. This study of the channel allows for an understanding of what places the channel differs from the ideal channel model described in Chapter I, and to what extent the experimental performance may deviate from the simulation results in Chapter II.

After gaining an understanding of the statistics of the channel, we calculate the bit error rates for each of the three scenarios. For scenarios I and II (SISO uncoded and Alamouti), it is observed that the experimental bit error rate is actually better than the simulated bit error rate. For the trellis code, however, the performance is much worse than what is expected, and it is probably likely that a more sophisticated decoding scheme may be necessary.

5.1 The Tones

The tones here are analyzed for the case where only the first four transmit antennas, as shown in Figure 3-3, are turned on. In this case, tones of 20 kHz, -40 kHz, 60 kHz, and 80 kHz were sent from antenna 1, antenna 2, antenna 3, and antenna 4, respectively. By accident, antenna 3 transmitted at a power 6 dBs higher than it should have been transmitting, and antenna 4 transmitted at a power 6 dBs lower than it should have been

transmitting. Antennas 1 and 2 transmitted correctly at equal power. The received signal at each receive antenna is a sum of these four tones modified by the channel coefficients to that receiver plus some noise. Figure 5-1 plots the received signal spectrum at baseband on a dB scale for all ten channels for the data in scenario 1 at normal SNR.

From the signal spectra, it is observed that all the tones are visible at every receive antenna, a sign that indicates all the channels are working properly. The variation of the magnitude of the tones at each receive antenna is a function of the differences in the subchannel from any specific transmit antenna to any specific receive antenna. In general, transmit antenna 3 has the best (strongest) channel while transmit antenna 4 has the worst (weakest) channel – this makes sense because transmit antenna 3 was transmitting at too high of a power and because transmit antenna 4 was transmitting at too low of a power. Whether transmit antenna 1 or 2 has a stronger channel, however, depends on the receive antenna.

Due to oscillator error, there is a slight offset (not apparent in Figure 5-1) in the frequency of the tone from what is expected. For the transmission burst whose tones are depicted in 5-1, this offset was calculated to be 341 Hz. This offset is the same over all receive antennas for a specific transmission burst because the same oscillator signal is used to drive all eight transmit antennas; however, the offset does vary over time, and must be re-estimated for each transmission burst. The variation of the offset over time reflects external changes or internal changes that affect the hardware. The offset was experimentally discovered to vary no more than 400 Hz.

In addition to the tones at 20 kHz, -40 kHz, 60 kHz, and -80 kHz, there are noisy tones, or "spurs" that are apparent at each receive antenna in 5-1. These "spurs" are the result of external or internal noise in the system, and, in general, their presence or lack thereof varies from receive antenna to receive antenna and from day to day; therefore there is no systematic way to remove them from the system. Fortunately, most of these noisy tones are removed by the application of the matched filter, which acts as a lowpass filter. Thus the only tones that remain are the ones within the bandwidth of interest (-82.944 kHz to 82.944 kHz).

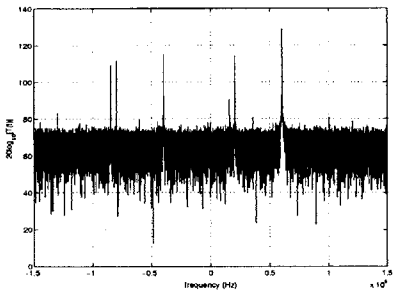

(a) Receive antenna 1

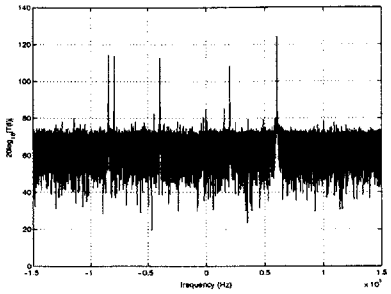

(b) Receive antenna 2

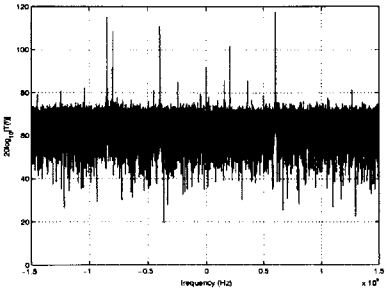

(c) Receive antenna 3

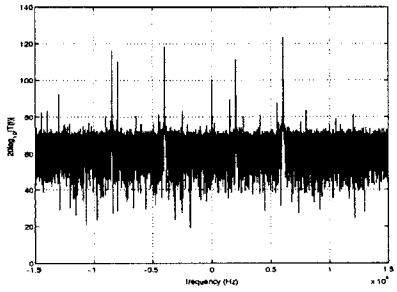

(d) Receive antenna 4

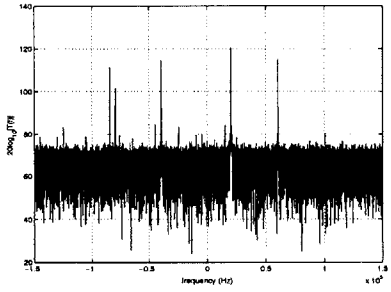

(e) Receive antenna 5

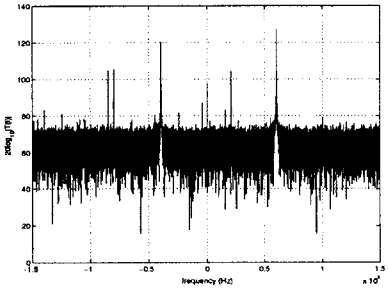

(f) Receive antenna 6

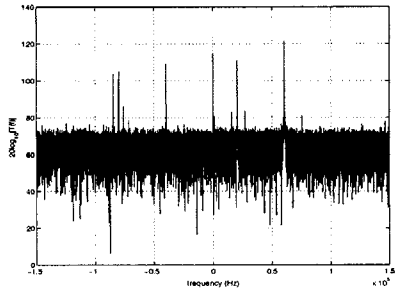

(g) Receive antenna 7

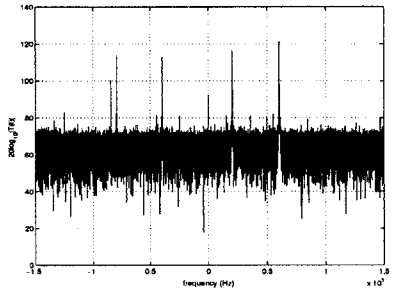

(h) Receive antenna 8

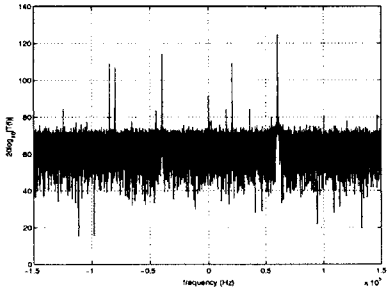

(i) Receive antenna 9

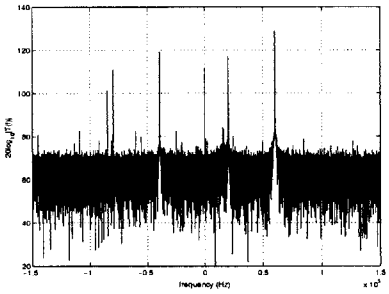

(j) Receive antenna 10

Figure 5-1: *Spectra of tones for ten receive antennas for scenario 1 data with only first four transmit antennas on*

5.2 The Noise

From analyzing the tones above, it was observed that there are two places that the ideal channel model differs from the experimental channel. First, there is the time-varying frequency offset due to oscillator error, and second, there is the presence of the noisy tones. The time-varying frequency offset is not a serious problem as long as the variation is slow enough that it can be accurately estimated it and corrected for. The noisy tones are also not a serious problem provided that there aren't too many of them at too high of an energy within the bandwidth of the system.

The presence of the noisy tones indicates that the noise in the system is clearly not AWGN. But, discounting the noisy tones, how AWGN is the noise? For each receive antenna, 10000 samples are available in the transmission burst structure to understand the noise characteristics at that antenna. During the portion of time these 10000 samples are collected, all eight transmit antennas are turned off. The purpose here is to understand:

- The noise in the phase at each receive antenna, which should be more or less uniform.
- The probability density function of the noise per dimension at each receive antenna, which should be more or less Gaussian.
- The temporal covariance function of the noise at each receive antenna, which should be more or less delta-like.
- The spatial covariance matrix, which should be pretty much diagonal.

Phase and Magnitude Characteristics of the Noise

Figure 5-2 shows the contour plot of the noise distribution on the complex plane, where darker regions correspond to more likely noise areas. As the figure shows, the phase noise does appear to be uniform, because the regions of decreasing density more or less extend out as circles of greater and greater radius around the point (0, 0); in other words, points that are of equal distance from the origin are pretty likely to fall into a region with the same coloration. This means that if the phase pdf were to be calculated by integrating along lines of different slope through the origin, it is expected that the integration would yield roughly the same value for any slope.

Of the ten receive antennas, from looking at Figure 5-2, it is seen that the probability density function of the phase noise for receive antennas 3, 7, and 10 would probably deviate the most from the uniform distribution.

To analyze the magnitude of the noise, it suffices to plot the probability density function of the distribution of the noise per dimension. From Figure 5-2, it is observed that the distribution along the imaginary and real dimension of the noise is about the same, so it is possible to separate the real and imaginary parts and plot a combined distribution of the noise values per dimension. This distribution is plotted in Figure 5-3, and for each receive antenna the best Gaussian fit (dotted lines) is also plotted on top. The best Gaussian fit is obtained by calculating the sample variance/dimension and mean for each receive antenna, which are the best unbiased estimators of the actual variance and mean [27].

Figure 5-3 shows that the noise can be well approximated as Gaussian at each receive antenna, particularly as the noise pdf moves away from the mean. There is some distortion near the mean: the distribution tends to overshoot the best Gaussian fit at the mean for most receive antennas.

The table below specifies the calculated sample variance and mean parameters per dimension for each receive antenna. The table also includes the sample variance per dimension at each receive antenna after a lowpass filter is applied around the bandwidth [-82.944 82.944] kHz. This is a more appropriate measure of the variance for the system because the decoding is performed after sampling at the output of the matched filter. After the lowpass filter, it is seen that the sample variance is clearly the worst for receive antennas 2, 3, and 4; receive antennas 6-10 have the best variances, and their variances are more or less the same.

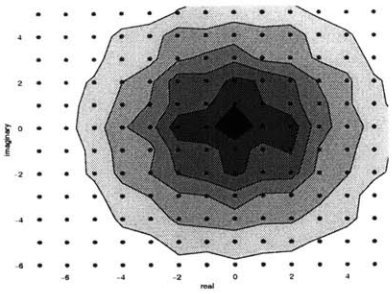

(a) Receive antenna 1

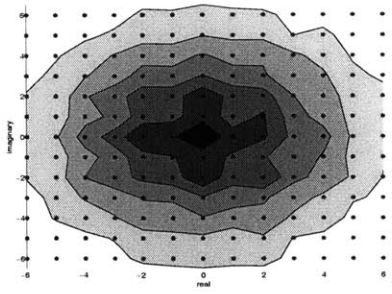

(b) Receive antenna 2

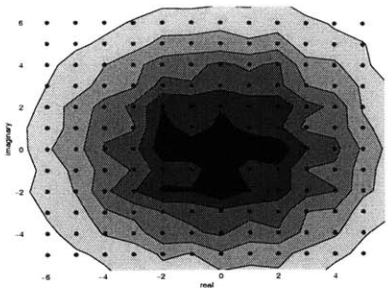

(c) Receive antenna 3

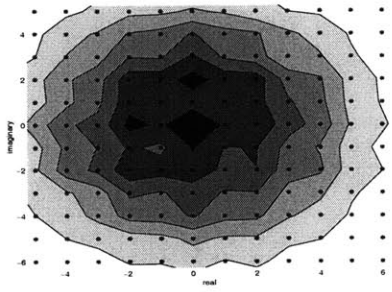

(d) Receive antenna 4

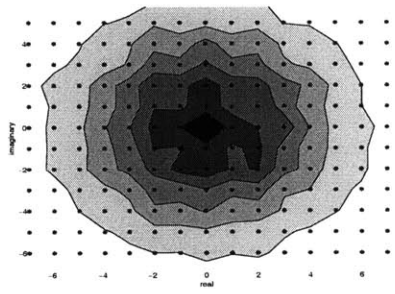

(e) Receive antenna 5

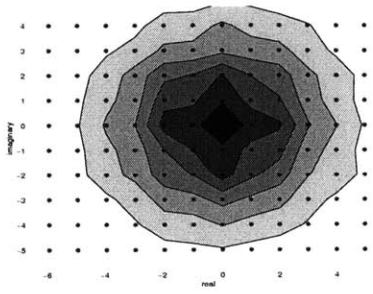

(f) Receive antenna 6

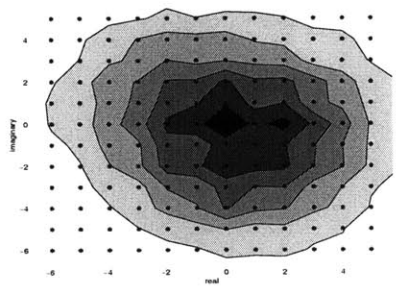

(g) Receive antenna 7

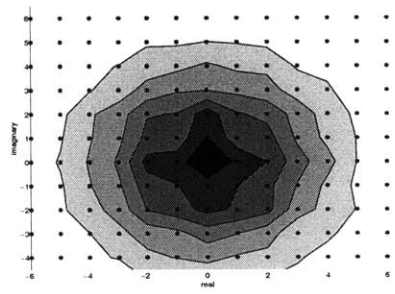

(h) Receive antenna 8

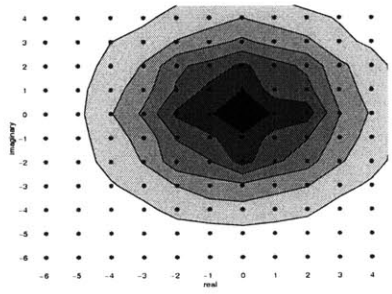

(i) Receive antenna 9

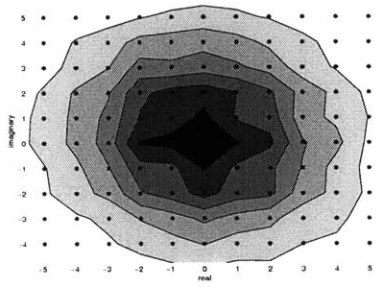

(j) Recieve antenna 10

Figure 5-2: *Contour plot of noise on complex plane*

Receive antenna	Sample Variance	Sample Mean	Sample Variance after Lowpass Filter
1	8.9142	.0021	.7886
2	10.9018	.0166	1.1964
3	11.2801	.0059	1.5530
4	9.2569	-.0525	1.5152
5	10.8987	-.0106	.9672
6	6.6701	-.0221	.5599
7	7.1721	-.0238	.6407
8	7.2381	-.0259	.5374
9	6.1842	.0399	.5444
10	6.009	.0514	.5700

5.2.1 Temporal and Spatial Noise Correlation

Next it is useful to analyze how white the noise is, both in time and in space. The temporal correlation can be obtained by simply calculating the autocorrelation function of the noise at each receive antenna, assuming the noise arises from a wide sense stationary process. In space, the spatial covariance matrix must be calculated.

The temporal autocorrelation function at each receive antenna is plotted in Figure 5-4. The function is plotted for the noise after it has been lowpass filtered around the bandwidth [-82.944 82.944] kHz. Receive antennas 1, 6, and 8 have the most white-like autocorrelation functions, while antennas 2, 3, 4, 7, and 10 have autocorrelation functions that indicate a great deal of correlation between adjacent samples. An interesting observation is that the degree of correlation for all receive antennas tends to fall off linearly as a function of sample spacing.

The absolute value of the spatial covariance matrix V after the application of the lowpass filter is given below:

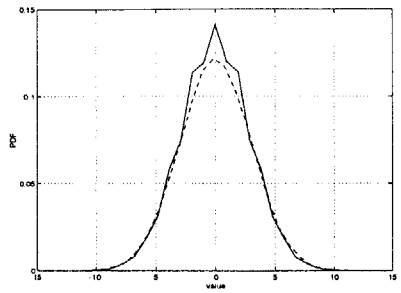

(a) Receive antenna 1

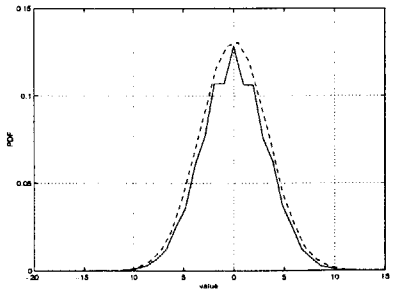

(b) Receive antenna 2

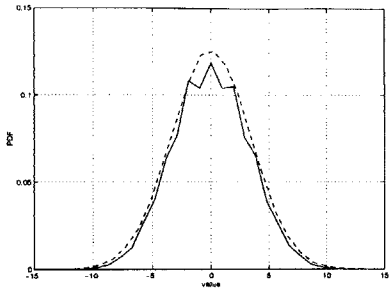

(c) Receive antenna 3

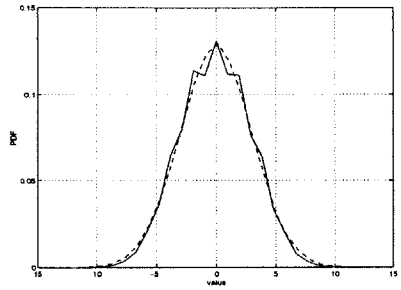

(d) Receive antenna 4

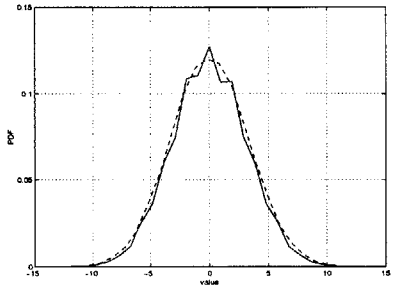

(e) Receive antenna 5

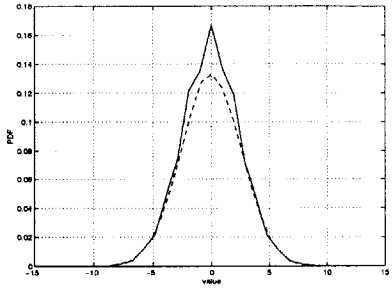

(f) Receive antenna 6

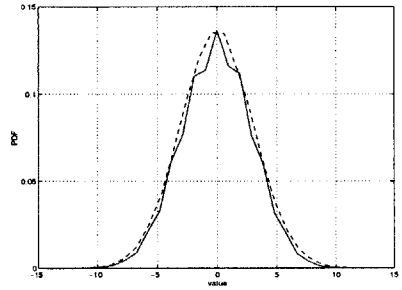

(g) Receive antenna 7

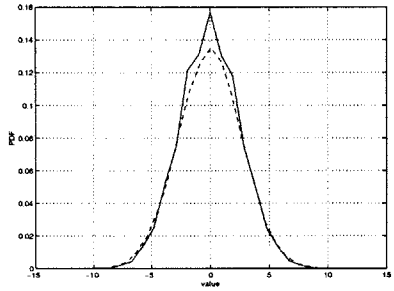

(h) Receive antenna 8

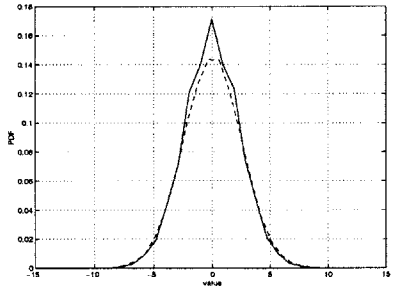

(i) Receive antenna 9

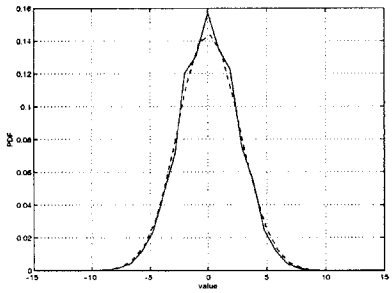

(j) Recieve antenna 10

Figure 5-3: *Plot of the probability distribution of the noise per dimension*

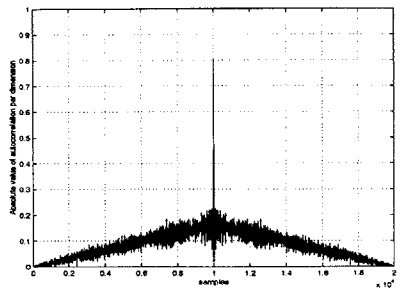

(a) Receive antenna 1

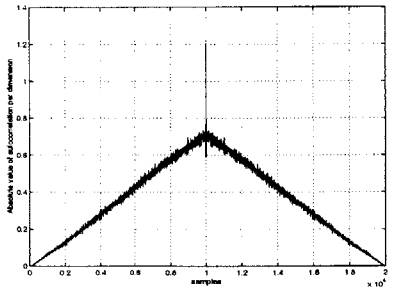

(b) Receive antenna 2

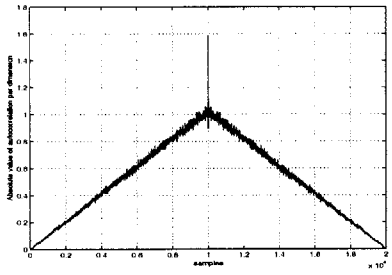

(c) Receive antenna 3

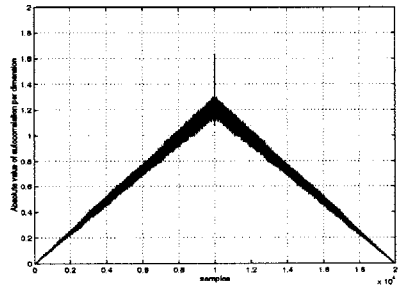

(d) Receive antenna 4

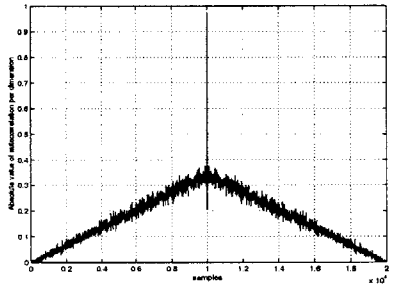

(e) Receive antenna 5

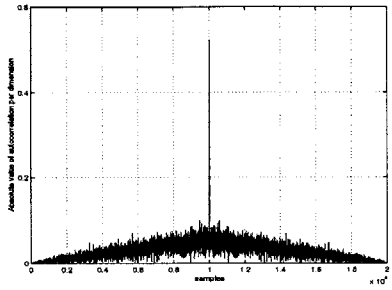

(f) Receive antenna 6

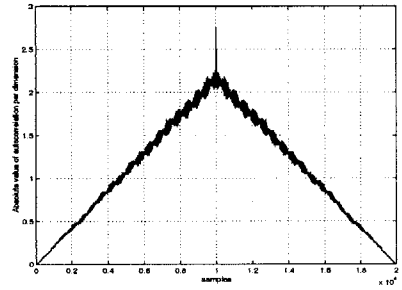

(g) Receive antenna 7

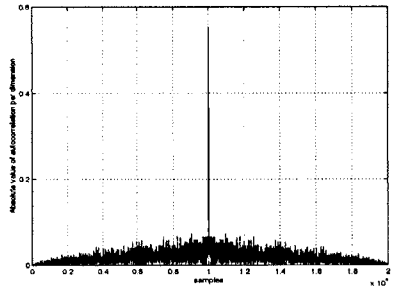

(h) Receive antenna 8

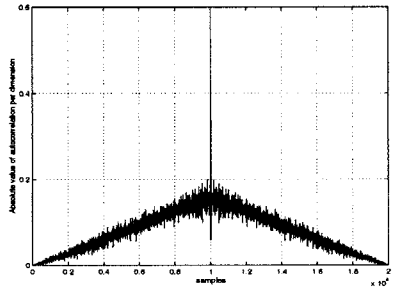

(i) Receive antenna 9

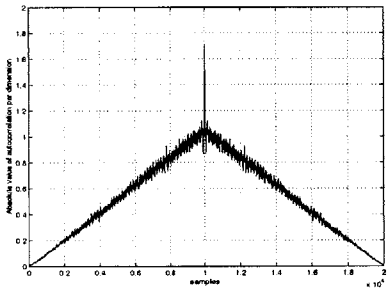

(j) Recieve antenna 10

Figure 5-4: *The absolute value of the noise temporal autocorrelation function per dimension for each receive antenna*

$$V = \begin{pmatrix} 0.7866 & 0.3297 & 0.3898 & 0.4432 & 0.2277 & 0.0868 & 0.1344 & 0.0747 & 0.1408 & 0.1000 \\ 0.3297 & 1.1964 & 0.8607 & 0.9213 & 0.5031 & 0.1849 & 0.2062 & 0.1341 & 0.3299 & 0.1717 \\ 0.3898 & 0.8607 & 1.5530 & 1.1252 & 0.5643 & 0.2306 & 0.2895 & 0.1764 & 0.3871 & 0.1807 \\ 0.4432 & 0.9213 & 1.1252 & 1.5152 & 0.6372 & 0.2410 & 0.3141 & 0.2063 & 0.4117 & 0.2149 \\ 0.2277 & 0.5031 & 0.5643 & 0.6372 & 0.9672 & 0.1379 & 0.1823 & 0.0970 & 0.2497 & 0.1431 \\ 0.0868 & 0.1849 & 0.2306 & 0.2410 & 0.1379 & 0.5199 & 0.0719 & 0.0243 & 0.0944 & 0.0525 \\ 0.1344 & 0.2062 & 0.2895 & 0.3141 & 0.1823 & 0.0719 & 0.6407 & 0.0667 & 0.1027 & 0.0954 \\ 0.0747 & 0.1341 & 0.1764 & 0.2063 & 0.0970 & 0.0243 & 0.0667 & 0.5374 & 0.0636 & 0.0430 \\ 0.1408 & 0.3299 & 0.3871 & 0.4117 & 0.2497 & 0.0944 & 0.1027 & 0.0636 & 0.5444 & 0.0661 \\ 0.1000 & 0.1717 & 0.1807 & 0.2149 & 0.1431 & 0.0525 & 0.0954 & 0.0430 & 0.0661 & 0.5700 \end{pmatrix}$$

The covariance matrix is not even close to diagonal. However, aside from the correlation between transmit antenna 4 and transmit antenna 3, there doesn't seem to be too much correlation between any of the receive antennas. The degree of (or lack thereof) correlation should be sufficient for the experiment.

5.3 Channel Estimation Sequences

The previous discussion on the noise characteristics of the system has served to demonstrate that the AWGN model is actually a pretty good estimate of real system noise. The only real deviation that can't be controlled for is the noisy tones that happen to fall within the bandwidth of interest, [-82.944 82.944] kHz.

The next part of the ideal channel model to be analyzed is the assumption of quasi-static fading. How stationary is the experimental channel? Intuitively, it is expected that the channel shouldn't fluctuate that much for a reasonable frame length because all the transmit and receive antennas have been fixed in place. The results of analyzing the channel estimation sequences indeed back up intuition.

5.3.1 Single Antenna Channel Estimation Sequences

As described in Figure 3-3, each single antenna channel estimation sequence is 5120 samples long, per transmit antenna. For each receive antenna, the received signal per transmit

antenna is split into 10 pieces of 512 samples each, and the channel is estimated over each piece. The estimation is performed by first lowpass filtering the received signal, then correlating with the actual transmitted channel estimation sequence, and sampling to obtain a sufficient statistic [27].

In Figure 5-5 the magnitude and phase of the channel estimates are plotted for transmit antennas 1-4. The channel estimates shown are plotted for receive antennas 1, 4, and 7 for the transmission burst corresponding to scenario 1 (SISO) at normal SNR; the plots are representative of the nature of the channel over all receive antennas over all transmission bursts.

The variation over time in the estimates has two causes: first, the variation of the actual channel, and second, the lack of precision in the estimates. From the results of the joint antenna channel estimation sequences in the subsection below, it will be seen that the lack of precision in the estimates is the reason for most of the variation seen in Figure 5-5.

From Figure 5-5, several conclusions may be drawn. First, because transmit antenna 3 is operating at a power level 6 dBs higher than it should be, the channel estimates for transmit antenna 3 are more or less uniformly higher at all receive antennas than the estimates for all other transmit antennas. In addition, because transmit antenna 3 is so strong, the channel estimates for that antenna appear much smoother: notice the phase estimates for transmit antenna 3 are pretty constant over time at each receive antenna.

On the other hand, transmit antenna 4, because it is operating at a power level 6 dBs less than normal, appears to have a wildly fluctuating channel. In reality, its channel is much more smooth, and this will be apparent from looking at the joint antenna channel estimates.

5.3.2 Joint Antenna Channel Estimation Sequences

From figure 3-3, 40960 samples are available at each receive antenna for estimating the channel jointly across all four transmit antennas. Because the joint antenna estimation sequences sent from the four transmit antennas form an orthogonal set, channel estimation can be performed in a similar manner to the estimation performed for the single antenna case, i.e. first lowpass filter, then matched filter, and last sample to obtain a sufficient statistic.

For each receive antenna, the received signal is broken up into ten pieces of 4096 samples,

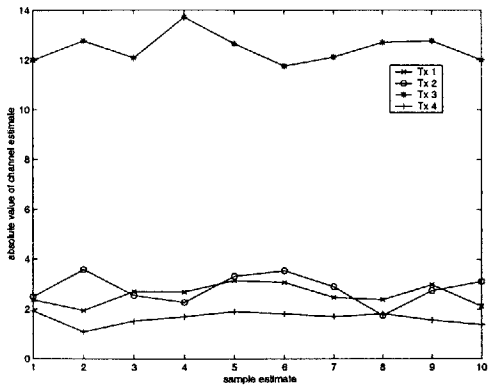

(a) Receive antenna 1, magnitude

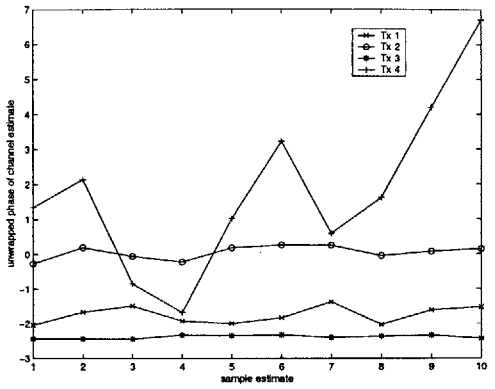

(b) Receive antenna 1, phase

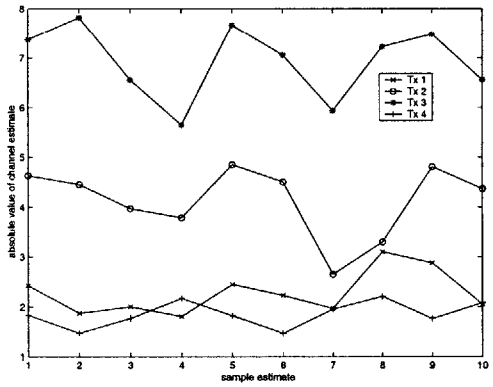

(c) Receive antenna 4, magnitude

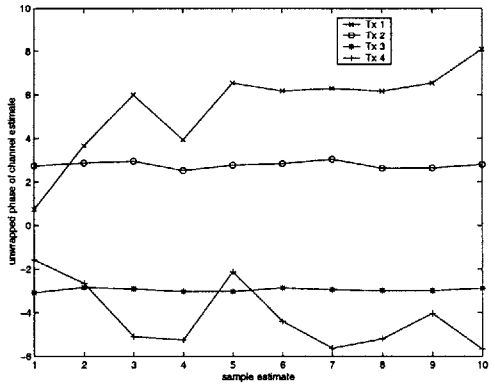

(d) Receive antenna 4, phase

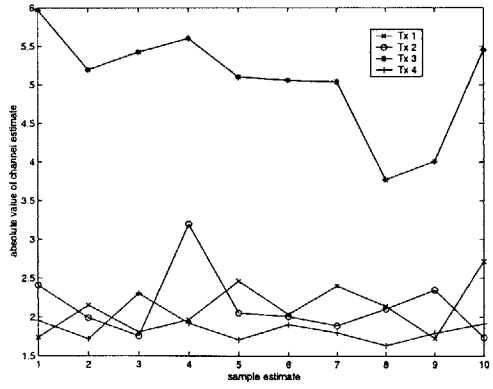

(e) Receive antenna 7, magnitude

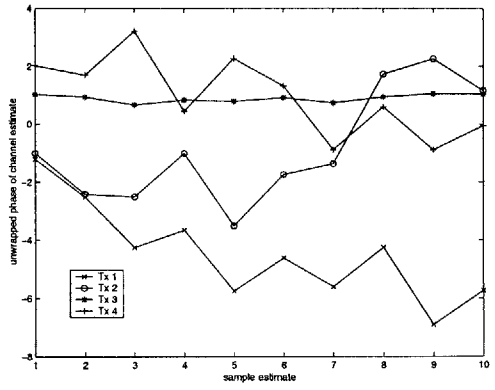

(f) Receive antenna 7, phase

Figure 5-5: *Magnitude and phase of single antenna channel estimates for transmit antennas 1-4 to receive antennas 1, 4, and 7 for sample transmission burst*

and the channel from all four transmit antennas is estimated for each piece. Because 4096 samples are available for each piece, as opposed to the 512 that were available with the single channel estimation sequeces, much more smooth and accurate channel estimates are possible. Figure 5-6 plots the results, once again for receive antennas 1, 4, and 7 for the transmission burst corresponding to scenario 1 (SISO) data at normal SNR.

The general results established for the single channel estimation sequences also apply here: namely, transmit antenna 3 has the best channel and transmit antenna 4 has the worst channel. The smoothness of the lack of significant variation of the channel estimates are a sign that the quasi-static fading model is indeed a pretty good approximation for the experiment.

5.4 SISO/Alamouti Performance

In this section the performance of an uncoded SISO 4-PSK system is analyzed and compared to the performance of the rate 1 Alamouti block code for two transmit antennas. Figures 5-7 and 5-8 show the performance achieved in each case for the Lincoln experiment, along with several reference curves. For the SISO case, receive antenna 8 was used, and for the Alamouti block code, receive antennas 8 and 9 were used. It was observed that after 11 dBs for the SISO case and after 8 dBs for the Alamouti case, the observed BER was uniformly 0.

In both cases the experimental curves are actually better than the simulated curves, and the Alamouti code results in a gain of about 1 to 2 dBs over the uncoded case. In the SISO case the curve actually is very close to curve that would be obtained over a Gaussian channel. This is an indication that the channel was fairly flat over the interval that the SISO data was being transmitted. The simulated curve in Figure 5-7 is worse than the experimental curve because the simulated curve takes into account all possible realizations of the channel, including the really bad ones that tend to dominate performance. However, during the experiment, it is not possible to probe all realizations of the channel; thus the performance appears better. The same argument explains why the Alamouti block code performs better in practice than in simulation.

Minimum mean squared channel estimation for the SISO and Alamouti cases was done in the following manner: An initial channel estimate was obtained by using the first frame

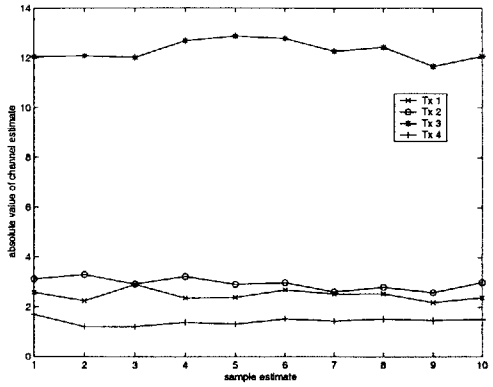

(a) Receive antenna 1, magnitude

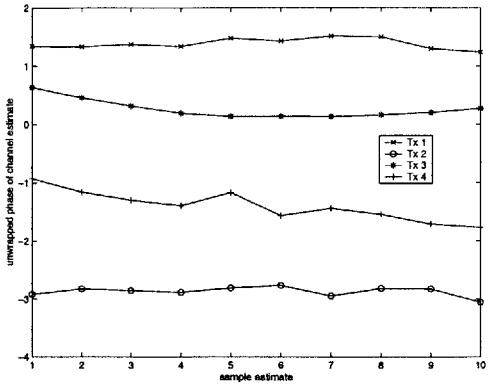

(b) Receive antenna 1, phase

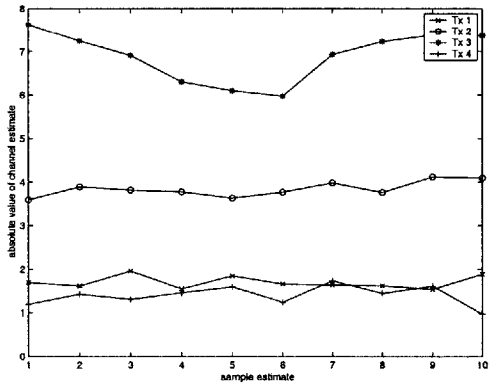

(c) Receive antenna 4, magnitude

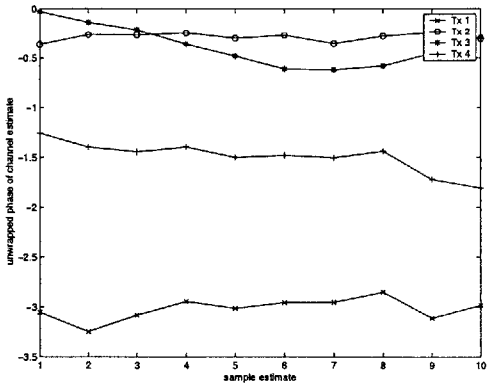

(d) Receive antenna 4, phase

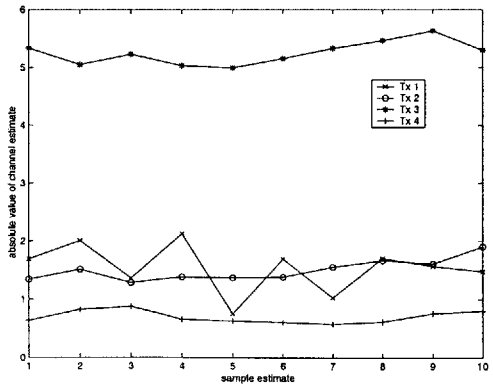

(e) Receive antenna 7, magnitude

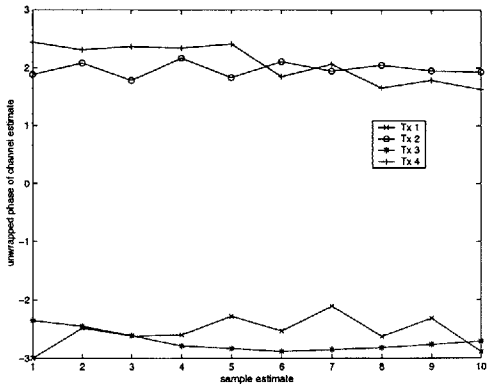

(f) Receive antenna 7, phase

Figure 5-6: *Magnitude and phase of joint antenna channel estimates for transmit antennas 1-4 to receive antennas 1, 4, and 7 for sample transmission burst*

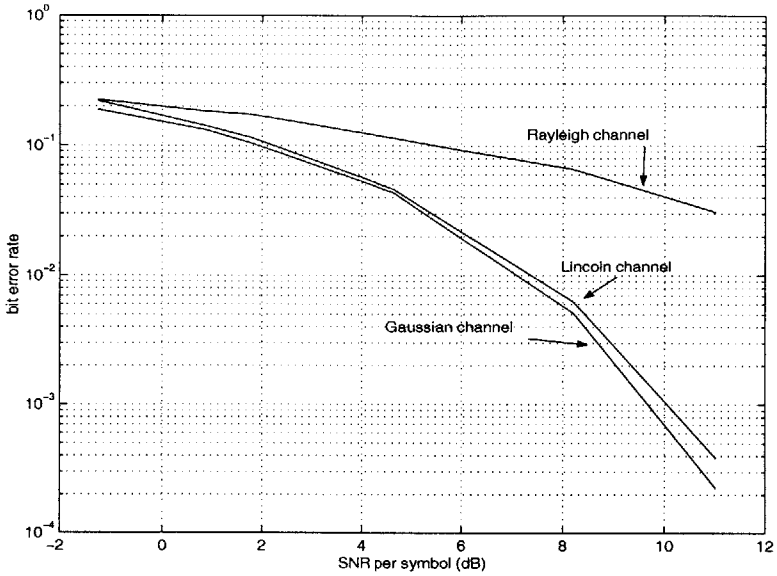

Figure 5-7: *Uncoded BER performance for SISO 4-PSK*

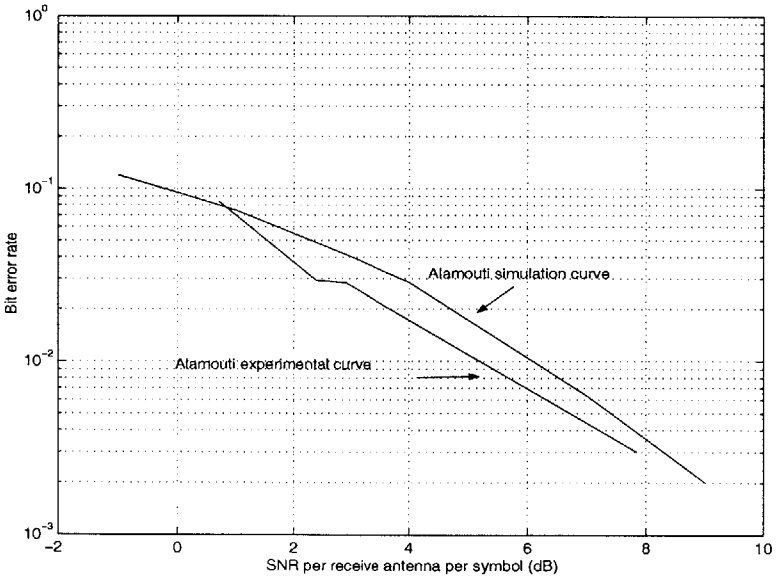

Figure 5-8: *Performance of Alamouti block code*

(in this case a frame represents 128 symbols) as a training sequence. The second frame was decoded by using the initial channel estimate. After this second frame was decoded, it was used as a training sequence to determine the channel over the interval it was actually transmitted. Given that the bit error rate is low enough, the process can be repeated to give better and better BER and channel estimates, although in practice the BER stagnates after 3 or 4 iterations. The resulting channel estimate is then used to decode the third frame, and so on.

Figure 5-9 plots some sample channel estimates for the SISO case at 4.7 dBs and 33.4 dBs. In both cases, the channel estimate is very smooth, as can be seen from the phase, although obviously at higher SNR the channel estimate is smoother. The periodicity in the phase is due to a misalignment with the oscillator frequency offset.

5.5 Future Work

In this thesis, a MIMO system has been designed to guage the effectiveness of space-time codes. Some preliminary analysis has also been done, and that analysis suggests that space-time codes are capable of achieving their theoretical potential. To establish that conclusion solidly, analysis of space-time block and trellis codes for the other scenarios listed in Chapter III must take place. In addition, it would be interesting to analyze the behavior of MIMO systems in the presence of another MIMO interferer [23], and to evaluate performance with error correction coding, using both hard and soft decisions.

In July, the Signals and Systems group at Lincoln Labs is undertaking a more sophisticated field test with moving transmit antennas and stationary receive antennas atop a garage at MIT. It would be interesting in this case to see how the quasi-stating fading assumption holds up in this more realistic channel, and whether and which space-time codes retain their power here too.

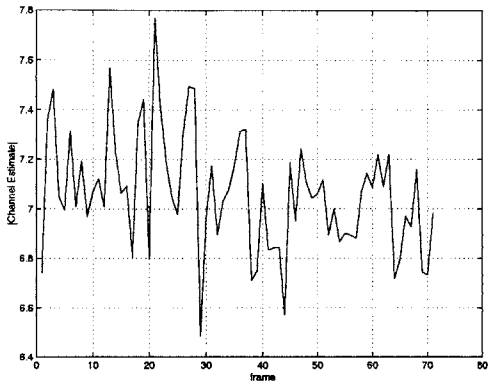

(a) SISO, 4.7 dBs, magnitude of channel estimate

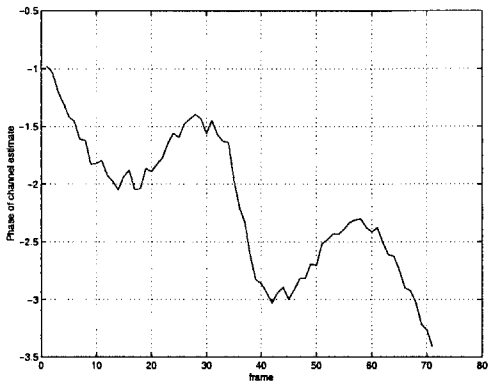

(b) SISO, 4.7 dBs, phase of channel estimate

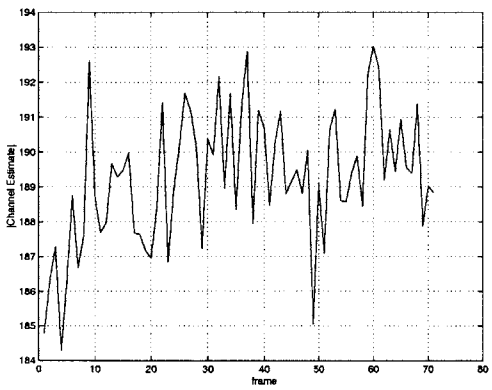

(c) SISO, 33.4 dBs, magnitude channel estimate

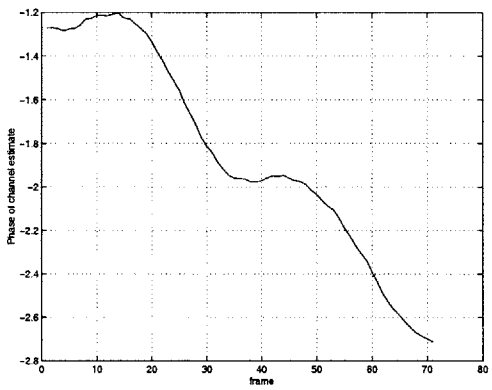

(d) SISO, 33.4 dBs, phase of channel estimate

Figure 5-9: *Magnitude and phase of channel estimates for SISO case at 4.7 and 33.4 dBs, respectively*

Bibliography

[1] C.M. Keller and D.W. Bliss, "Cellular and PCS propagation measurements and statistical models for urban multipath on an antenna array," *Proceedings of the 2000 IEEE Sensor Array and Multichannel Signal Processing Workshop, Cambridge, MA.*, Mar. 2000, p. 32-36

[2] C. C. Martin, J. H. Winters, N. R. Sollenberger, "Multiple-input multiple-output (MIMO) radio channel measurements," Antennas and Propagation Society, 2001 IEEE International Symposium, vol. 1, 2001, p. 418-421.

[3] A. Lee Swindlehurst, G. German, J. Wallace, M. Jensen, "Experimental Measurements of Capacity of MIMO Indoor Wireless Channels," Third IEEE Signal Processing Workshop on Signal Processing Advances in Wireless Communications, Taoyuan, Taiwan, Mar. 20-23, 2001.

[4] G. D. Golden, G. J. Foschini, R. A. Valenzuela, and P.W. Wolniansky, "Detection algorithm and initial laboratory results using the V-BLAST space-time communication architecture," *IEEE Electronics Letters*, vol. 35, No. 1, Jan. 7, 1999, p. 14-15.

[5] E. Telatar, "Capacity of multi-antenna Gaussian channels," AT&T-Bell Labs Internal Tech. Memo., June 1995.

[6] G.J. Foschini and M.J. Gans, "On limits of wireless communications in a fading environment when using multiple antennas," *Wireless Personal Communications*, pp. 311-335, 1998.

[7] J. Kusuma, "A simple coded-modulation approach to multi-antenna systems," Presented at the 2002 Conference on Information Sciences and Systems.

[8] A.J. Viterbi, J.K. Wolf, E. Zehavi, and R. Padovani, " A pragmatic approach to trellis-coded modulation," *IEEE Communications Maganize 27*, 1989, p. 11-19.

[9] , G. Ungerboeck, "Channel coding with multilevel/phase signals", *IEEE Transactions on Information Theory* IT-28, 1982, p. 55-67.

[10] V. Tarokh, N. Seshadri, and A.R. Calderbank, "Space-time codes for high data rate wireless communication: performance criterion and code construction," *IEEE Transactions on Information Theory*, vol 40, pp. 744-765, March 1998.

[11] Z. Chen, J. Yuan, and B. Vucetic, "Improved space-time trellis coded modulation scheme on slow Rayleigh fading channels," *IEEE Electronics Letters*, vol. 37, p. 440-441, Mar. 2001.

[12] Z. Chen, Branka S. Vucetic, Jinhong Yuan, and Ka Leong Lo, "Space-Time trellis codes for 4-PSK with three and four transmit antennas in quasi-static flat fading channels," *IEEE Communications Letters*, vol. 6, p. 67-69, Feb. 2002.

[13] S. Alamouti, "A simple transmit diversity technique for wireless communications", *IEEE Journal on Select Areas in Communications*, vol. 16, p. 1451-1458, Oct. 1998.

[14] V. Tarokh, H. Jafarkhani, and A. R. Calderbank, "Space-time block coding for wireless communications: performance results," *IEEE Journal on Selected Areas in Communications*, vol. 17, p. 451-460, Mar. 1999.

[15] V. Tarokh, H. Jafarkhani, and A.R. Calderbank, "Space-time block codes from orthogonal designs," *IEEE Transactions on Information Theory*, vol. 45, p. 1456-1467, July 1999.

[16] X. Li, T. Luo, G. Yue, and C. Yin, "A squaring method to simplify the decoding of orthogonal space-time block codes," *IEEE Transactions on Communications*, vol. 49, p. 1700-1703, Oct. 2001.

[17] S. Baro, G. Bauch, and A. Hansmann, "Improved codes for space-time trellis-coded modulation," *IEEE Communications Letters*, vol. 4, p. 20-22, Jan. 2000

[18] A. Wittneben, "A new bandwidth efficient transmit antenna modulation diversity scheme for linear digital modulation," in *Proc. IEEE'ICCC*, p. 1630-1634, 1993

[19] Proakis, John G, *Digital Communications*, McGraw Hill Inc. New York, NY 2001.

[20] P. A. Laurent, "Exact and approximate construction of digital phase modulations by superposition of amplitude modulated pulses (AMP)," *IEEE Transactions on Communications*, Vol. COM-34, No. 2, Feb. 1986.

[21] X. Zhang and M.P. Fitz, "Space-time code design with CPM transmission," *ISIT 2001*, Washington, D.C., June 24-29, 2001

[22] K.W. Forsythe, D.W. Bliss, and C.M. Keller, "Multichannel adaptive beamforming and interference mitigation in multiuser CDMA systems," *Conference Record of the Thirty-Third Asilomar Conference on Signals, Systems & Computers, Pacific Grove, Calif.*, vol. 1, p. 506-510, Oct. 1999.

[23] V. Tarokh, A. Naguib, N. Seshadri, and A. Robert Calderbank, "Combined array processing and space-time coding," *IEEE Transactions on Information Theory*, vol. 45, p. 1121-1128, May 1999

[24] Personal conversation with Dr. A.F. Yegulalp, staff member in the Sensor Exploitation group at MIT Lincoln Laboratory, 244 Wood St., Lexington, MA, June 2002, *yegulalp@ll.mit.edu.*

[25] http://www.ee.byu.edu/ee/class/ee444/simulink/usdc/rcnotes.pdf.

[26] http://www.mathworks.com/access/helpdesk/help/toolbox/signal/tukeywin.shtml.

[27] G. Wornell and A. Willsky, *Stochastic Processes and Detection: Class Notes*, spring 2002.